4 Laboratory of Genome Dynamics in the Immune System, Labellisé Ligue, INSERM UMR 1163, Université de Paris, Institut Imagine, Paris, France
5 Platform for Metabolic Analyses, Structure Fédérative de Recherche Necker, INSERM US24/CNRS UMS 3633, Paris, France
6 Functional Genomics of Solid Tumors Team, Centre de Recherche des Cordeliers, INSERM, Sorbonne Université, Université de Paris, Université Paris 13, Labex Immuno-Oncology, Équipe Labellisée Ligue Contre le Cancer, Paris, France
7 Université Côte d'Azur, INSERM, U1065, C3M, CHU, Nice, France
8 Institute of Molecular Oncology and Functional Genomics, Rechts der Isar University Hospital, Munich, Germany
9 Research Unit of Radiation Cytogenetics, Helmholtz Zentrum München, Neuherberg, Germany.
10 Service d'Anatomie Pathologique, Hôpital Beaujon, Assistance Publique-Hôpitaux de Paris, Clichy, France

§ / $ These authors contributed equally to this work

*Corresponding author: Chantal Desdouets - Centre de Recherche des Cordeliers, INSERM UMRS 1138, Team "Proliferation, Stress and Liver Physiopathology", 75006 Paris, France.
Email: chantal.desdouets@inserm.fr.

No conflict of interest

IN BRIEF

Donne *et al.* identify that NAFLD hepatocytes display hallmarks of replication stress, due to a nucleotide pool imbalance. Replication stress is sufficient to elicit NAFLD hepatocyte DNA lesions and to drive activation of the DNA-sensing pathway, cGAS-STING.

HIGHLIGHTS

- Proliferating NAFLD hepatocytes harbor replication stress
- Defective replication fork dynamic induces DNA damage signaling
- Nucleotide pool imbalance promotes replication stress in NAFLD hepatocytes
- The cGAS-STING pathway connects DNA damage to interferon pathway in NAFLD hepatocytes

LIMITATION OF THE STUDY

While our study shows that proliferating murine NAFLD hepatocytes exhibit replication stress and DNA damage, one of the NAFLD mouse models present severest DNA lesions. Additional studies examining the nature of these DNA lesions in the two NAFLD models are warranted as well as their contribution during NAFLD development. Nucleotide pool imbalance is a key feature of NAFLD and contributes to replication stress in steatotic hepatocytes. We were not able to identify whether nucleotide supplementation prevents disease progression in mouse models of NAFLD. This question will be the focus of future studies. It would also be particularly pertinent to define whether cGAS-STING activation in NAFLD hepatocytes may prevent or participate to NAFLD-associated HCC development.

SUMMARY

Non-alcoholic steatotic liver disease (NAFLD) is the most common cause of chronic liver disease worldwide. NAFLD has a major effect on the intrinsic proliferative properties of hepatocytes. Here, we investigated mechanisms underlying activation of the DNA damage response during NAFLD. Proliferating mouse NAFLD hepatocytes harbor replication stress with an alteration of the replication fork's speed and activation of ATR pathway which is sufficient to cause DNA breaks. Nucleotide pool imbalance occurring during NAFLD is the key driver of replication stress. Remarkably, DNA lesions drive cGAS/STING pathway activation, a major component of cells' intrinsic immune response. The translational significance of this study was reiterated by showing that lipid overload in proliferating HepaRG was sufficient to induce replication stress and nucleotide pool imbalance. Moreover, livers from NAFLD patients displayed nucleotide pathways deregulation and cGAS/STING genes alteration. Altogether, our findings shed new light on the mechanisms by which damaged NAFLD hepatocytes might promote disease progression.

KEYWORDS

Hepatocyte, Non-Alcoholic Fatty Liver Disease, Cell proliferation, DNA damage, Replication stress, dNTP pools, cGAS/STING.

Introduction

Obesity and diabetes are now considered to be pandemic social and economic burdens. The liver is one of the key organs affected by these conditions, resulting in non-alcoholic steatotic liver disease (NAFLD) (Anstee et al., 2019, 2013; Diehl et al., 2019; Eslam et al., 2020; Friedman et al., 2018; Younossi et al., 2018). NAFLD is characterized by excessive triglyceride accumulation in hepatocytes in the absence of significant alcohol consumption. The prevalence of NAFLD is currently estimated at 25% in the general population (Estes et al., 2018; Younossi et al., 2016). NAFLD encompasses a spectrum of liver conditions ranging from simple hepatic steatosis or non-alcoholic steatotic liver (NAFL) to the concomitant presence of hepatocellular damage (ballooning), Mallory-Denk body formation, and lobular necro-inflammation, defining non-alcoholic steatohepatitis (NASH), which can lead to various degrees of additional fibrosis (Brunt et al., 1999; Brunt and Kleiner, 2017; Kleiner et al., 2005; Singh et al., 2015). The risk of adverse outcomes is low for NAFL, whereas NASH can progress to more severe stages, such as cirrhosis and hepatocellular carcinoma (HCC) (Anstee et al., 2019; Fingas et al., 2016). NAFLD is currently driving an alarming increase in the incidence and prevalence of HCC in developed and developing countries, and it has been predicted that NAFLD will become the most common underlying etiological risk factor for HCC and liver transplantation in the future (Baffy et al., 2012; Wang et al., 2014; Wong et al., 2014).

NAFLD is a complex disease, the development and progression of which require multiple parallel hits (dietary habits, environmental factors) in genetically predisposed individuals (Buzzetti et al., 2016; Diehl and Day, 2017; Friedman et al., 2018; Taliento et al., 2019; Tilg and Moschen, 2010; Valenti and Baselli, 2018). One of the main mechanisms observed in NAFLD pathogenesis is hepatocyte lipotoxicity. While

triglyceride accumulation is believed to be relatively benign (e.g. steatosis), hepatocyte lipotoxicity is thought to be chiefly caused by free steatotic acids and their metabolites (Donnelly et al., 2005; Friedman et al., 2018; Mota et al., 2016). These changes within the liver place extra metabolic stress on various organelles, such as the mitochondria and endoplasmic reticulum, triggering a cascade of stress-induced responses, including the generation of reactive oxygen species (ROS) (Begriche et al., 2013; Kim et al., 2018; Lebeaupin et al., 2018). This leads to further cell injury, culminating in inflammation, programmed cell death (apoptosis), and fibrotic remodeling (Anstee et al., 2019; Schwabe and Luedde, 2018; Wolf et al., 2014). The progression or resolution of NASH depends on the balance between cell injury and regeneration (Wegermann et al., 2018). Interestingly, high levels of lipogenesis, liver damage, and immune infiltration have been identified as key drivers of the development of murine HCC (Gomes et al., 2016; Nakagawa et al., 2014; Wolf et al., 2014).

NAFLD has a major effect on the intrinsic proliferative properties of hepatocytes (Collin de l'Hortet et al., 2014; Leclercq et al., 2006; Richardson et al., 2007; Yang et al., 2004). The hepatocytes of NAFLD patients express senescence markers such as p21, short telomeres, large numbers of senescence-associated DNA damage foci, and larger nuclei (Aravinthan et al., 2013; Donati et al., 2017; Gentric et al., 2015; Nakajima et al., 2010; Ogrodnik et al., 2017). Interestingly, studies in animals have shown that a decrease in the number of senescent cells reduces overall hepatic steatosis (Ogrodnik et al., 2017). Oxidative DNA damage also affects the division of NAFLD hepatocytes. Such damage is more pronounced in the livers of NASH patients developing HCC than in those without HCC (Nishida et al., 2016; Tanaka et al., 2013). In mouse models of NASH, oxidative stress activates the DNA damage response (DDR) in dividing steatotic hepatocytes (Gentric et al., 2015; Gentric and Desdouets, 2015).

Compensatory proliferation and DNA damage are key determinants of cancer development in patients with chronic liver disease, notably in the context of NAFLD (Boege et al., 2017). Although several studies provided evidence that aberrant metabolism, inflammatory microenvironment, and compensatory hepatocyte proliferation (Gomes et al., 2016; Nakagawa et al., 2014; Wolf et al., 2014) are key features in NASH-HCC pathogenesis, it is still important to determine the major molecular events underlying activation of the DNA damage response during NAFLD. Here, we show that proliferating NAFLD hepatocytes harbor a global perturbation of the DNA replication program highlighted by a disruption of replication forks' speed and activation of ATR/CHK1 pathway. Consequently, replication-associated DNA lesions accumulate in NAFLD hepatocytes. Our finding also demonstrate that nucleotide pool imbalance is a key feature of NAFLD and contributes to replication stress in steatotic hepatocytes. Finally, we show that DNA lesions in NAFLD hepatocytes drive activation of the cGAS/STING pathway, a major component of cells' intrinsic immune response.

Results

Proliferating NAFLD hepatocytes experience replication stress

We hypothesized that DDR activation in NAFLD could be induced by the disturbance of replication dynamics. To address this point, we used two well-described mouse models of NAFLD: C57BL/6J mice fed a high-fat high-sucrose diet (HFHS) (Verbeek et al., 2015) or a choline–deficient high-fat diet (CDHFD) (Wolf et al., 2014). As expected, mice fed a HFHS diet or a CDHFD for six months were heavier than mice fed a standard diet (SD) (Fig. S1 A). Analyses of H&E liver sections revealed that NAFLD diets consistently led to mixed macro-mediovesicular, predominantly centrilobular steatosis (Fig. S1 B). NAFLD activity score (NAS) was significantly higher in the livers of mice fed the CDHFD than in those of mice fed the HFHS diet, due to the presence of marked steatosis and lobular inflammation (Fig. S1 B, C and D). Then, we analyzed different replication parameters by using primary hepatocyte culture isolated from SD and NAFLD livers (HFHS and CDHFD), which is known to be a relevant *ex vivo* model to study cell division (Fig. 1 A) (Gentric et al., 2015; Hsu et al., 2016; Margall-Ducos et al., 2007; Wirth et al., 2006). As previously described, freshly isolated hepatocytes seeded in growth media initiated G1 phase, and then progressed into S-phase after 36 hours (Duncan et al., 2010; Fortier et al., 2017; Gentric et al., 2015). Replication can be tracked by the addition of thymidine analogs into the medium as BromodeoxyUridine (BrdU). The percentage of BrdU-positive cells in the HFHS/CDHFD population was similar to control cells between 36 and 48 hours but was significantly higher at 60 hours suggesting that NAFLD hepatocytes may have difficulty to replicate their genome (Fig. S2 A and B). The analysis of the expression of cyclin A (*Ccna2*), a master regulator of progression through the S phase (Norbury et al., 1991), supported evidence for prolonged S-phase (Fig. S2 C). As previously

published (Gentric et al., 2015), nuclear phospho-histone H3 (pHH3) staining showed that NAFLD hepatocytes also accumulated in G2/M phase (Fig. S2 D and E). To better understand the phenotype of prolonged S phase, we asked whether NAFLD hepatocytes have difficulties replicating their genome. The replication dynamic was evaluated by measuring DNA replication fork progression on single DNA molecules stretched by DNA combing (Mokrani-Benhelli et al., 2013). For this purpose, proliferating hepatocytes were subjected to double-labeling with successive pulses of the thymidine analogs 5-chloro-2'-deoxyuridine (CldU) and 5-iodo-2'-deoxyuridine (IdU) (Fig. 1 B). DNA fiber imaging and quantification revealed that HFHS and CDHFD hepatocytes had shorter nascent DNA tracks than SD hepatocytes (Fig. 1 B and C), demonstrating the existence of a replication stress (RS) in these cells (Aguilera and García-Muse, 2013; Gaillard et al., 2015; Magdalou et al., 2014; Techer et al., 2017). Interestingly, HFHS hepatocytes present a lower fork velocity than CDHFD (Fig. 1 B and C). ATR (ataxia telangiectasia and Rad3-related) plays a key role in the response to replication stress and acts as an S-phase checkpoint protein kinase (Saldivar et al., 2017). The principal signal triggering ATR activation is replication protein A (RPA)-coated ssDNA (Toledo et al., 2013). Once activated, ATR coordinates cell cycle progression, replication fork protection, repair and restart mechanisms through the phosphorylation of specific targets, such as the CHK1 effector kinase and RPA itself (pCHK1^{s317} and pRPA32^{s33}, respectively). Consistent with an activation of the replication stress response, we observed a sharp increase in the phosphorylation of CHK1 and RPA32 in HFHS and CDHFD primary hepatocytes, whereas this signal was barely detectable in SD cells (Fig. 1 D and E). We further explored the transcriptome, and performed pathway profiling for genes differentially expressed between dividing NAFLD and control hepatocytes. Gene set enrichment analysis (GSEA) identified

multiple pathways involved in cell cycle checkpoints, such as the G2/M checkpoint, p53 signaling and DNA repair, among the top-ranking genes differentially expressed (Fig. 1 F). Importantly, we confirmed the association between a replication stress gene signature and the upregulated genes in proliferating HFHS/CDHFD hepatocytes, including genes encoding DNA lesion recognition and DNA repair proteins (Fig. 1 G). Quantitative PCR analyses also demonstrated upregulation of genes involved in nucleotide excision repair (NER) (*Xpf*, *Xpc*, *Ercc1*), the repair of oxidized bases (*Neil*, *Ogg1*), homologous recombination (*Brca1*, *Rad51*) and DNA lesion signaling (*Gadd45a*, *Fancl*) in NAFLD hepatocytes (Fig. 1 H). Overall, our findings show that NAFLD hepatocytes harbored replication stress, leading to an activation of the ATR/CHK1 pathway.

Replication stress drives DNA damage in NAFLD hepatocytes.

We next investigated whether *in vivo* compensatory proliferation occurring during NAFLD was a source of DNA damage in proliferating hepatocytes. Co-staining for γH2AX (H2A.X variant histone) and PCNA (Proliferating Cell Nuclear Antigen) was performed on liver sections from our models (Fig. 2 A). A slight increase of PCNA-positive hepatocytes was observed in HFHS and CDHFD liver parenchyma (Fig. S2 F), reflecting as reported, compensatory proliferation in NAFLD tissue (Boege et al., 2017). Damaged hepatocytes represent 5% of total hepatocytes in NAFLD livers while they represent less than 0.2% in healthy livers (Fig. S2 G). Interestingly, it is noteworthy that most proliferating NAFLD hepatocytes were also stained for γH2AX compared to SD hepatocytes (Fig. 2 B). As replication stress is a major source of chromosomal lesions (Gaillard et al., 2015), we explored the presence of DNA damage in replication stress experienced NAFLD dividing hepatocytes. γH2AX was barely detectable in

control hepatocytes whereas high levels were detected in HFHS/CDHFD hepatocytes, particularly at 60 hours, when NAFLD hepatocytes were experiencing the replication stress (Fig. 2 C and D). Co-immunostaining of γH2AX and pHH3 confirmed this result by showing that pHH3-positive NAFLD nuclei had higher γH2AX levels than pHH3-negative nuclei (Fig. 2 E and F). These data indicate that NAFLD hepatocytes accumulate replication-associated DNA damage during replication and G2/M. To further explore the type of accumulated DNA damage, alkaline comet assays were performed. These assays detect DNA double (DSB) and/or single-strand (SSB) breaks, by measuring nuclear DNA tails after electrophoresis. We did not observe nuclear tails in SD nuclei (Fig. 2 G). By contrast, HFHS and CDHFD nuclei presented extensive DNA strand breaks; these lesions being more pronounced in CDHFD hepatocytes (Fig. 2 G). Finally, we quantified 53BP1 foci, an established mediator of DSB repair (Fig. 2 H). At least 4 foci per nucleus are considered as a mark of spontaneous DSB lesions (Lukas et al., 2011). We observed a small number of 53BP1 nuclear bodies in SD and HFHS hepatocytes while 40% of CDHFD hepatocytes presented nuclei with a high number of 53BP1 nuclear bodies (Fig. 2 H and I). Collectively, these results demonstrate that replication stress is sufficient to elicit hepatocyte DNA lesions in the context of NAFLD. Finally, we investigated whether lipid overload is able to trigger replication stress and signs of DNA damage. We used the metabolically competent differentiated human hepatocyte-like cell line HepaRG (ΔHepaRG). This model has a particular relevance to study the onset of NAFLD, in which hepatocytes undergo lipid metabolism remodeling and accumulate intracellular lipid droplets (Rappez et al., 2021). ΔHepaRG cells were stimulated with oleic and palmitic steatotic acids (FA condition) to model NAFLD-specific lipid metabolism (Malehmir et al., 2019; Wolf et al., 2014) (Fig. S3 A). As expected, lipid accumulation

was visible in FA-treated cells on neutral oil red O staining (Fig. S3 B). Interestingly, RNA sequencing analysis showed a multitude of upregulated pathways notably involved in replication processes in the FA condition compared to untreated cells (UT) (Fig. S3 C). Parameters of replication and DNA damage were next assessed. The FA-treated cells displayed a slower progression of replication forks (Fig. S3 D) associated to the accumulation of DNA damage evaluated by comet assays and γH2AX expression (Fig. S3 E, F and G). These results demonstrate that lipid overload in proliferating human hepatocytes leads to replication stress and consequently to DNA damage.

Alteration of the nucleotide pool results in DNA replication stress during NAFLD. Obstacles to replication fork progression can arise from several endogenous or exogenous sources, ranging from a depletion of the nucleotide pools available for DNA synthesis to transcription-replication machinery collisions, the formation of RNA-DNA hybrids, and oncogene-induced increases in replication origin firing (Techer et al., 2017). Extensive metabolic reprogramming occurs during the pathogenesis of NAFLD. We investigated whether metabolic disturbances interfered with the replicative machinery in this context. We performed targeted metabolomic analyses by tandem liquid chromatography-mass spectrometry (LC-MS) on mouse livers. As expected, the development of NAFLD led to metabolic reprograming in HFHS/CDHFD livers (Fig. 3 A and B). Interestingly, we observed a significant change in purine and pyrimidine metabolism in HFHS and CDHFD livers relative to SD livers, reflecting nucleotide deregulation (Fig. 3 A and B). In the same way, our transcriptomic analysis of replicating NAFLD hepatocytes revealed an enrichment in genes linked to nucleotide biosynthesis among the downregulated genes in these cells (Fig. S4A). Accordingly,

LC-MS showed that replicating NAFLD hepatocytes had an imbalanced nucleotide pool (Fig. 3 C and S4 B and C). Monophosphate and diphosphate nucleotides accumulated in NAFLD hepatocytes (Fig. S4 D and E). By contrast, the cellular concentrations of deoxyadenosine triphosphate (dATP) and deoxythymidine triphosphate (dTTP) were low in these cells (Fig. 3 D and S4 F). The nucleotide pool is known to be a limiting factor for the correct progression of replication (Poli et al., 2012). To investigate the connection between the nucleotide pool imbalance and the replication stress we provided additional dNTPs in the culture media, during the replication of primary hepatocytes. First, we did not observe any impact of dNTPs supply in SD hepatocytes on the replication dynamic and DNA damage (Fig. 3 E, F, G, H and I). However, dNTPs treatment ameliorated the fork velocity of proliferating HFHS hepatocytes (Fig. 3 E) as well as it decreased accumulation of DNA damage (Fig. 3 F, G, H, I and Fig. S4 G) suggesting that dNTP supplementation diminishes DNA damage by counteracting DNA replication defects. Interestingly, treatment of proliferating CDHFD hepatocytes with the dNTPs reduced accumulation of DNA damage (Fig. 3 F, G, H, I and Fig. S4 G) but also reduced the fork velocity (Fig. 3 E), suggesting a decoupling of the replication and repair systems. The translational significance of these results was reiterated by showing that lipid overload in proliferating ΔHepaRG was sufficient to provoke dNTPs imbalance. In fact, FA-treated cells present a dysregulation in purine and pyrimidine pathways (Fig. S3 H) as well as a decrease of dATP and dTTP (Fig. S3 I). Finally, we investigated whether a nucleotide pool imbalance occurs in the human pathogenesis of NAFLD. Patients were selected and divided into three groups: healthy, steatotic and NASH. The clinical and histological details of the patients are summarized in Table 1. Quantification of metabolites was performed on resected liver tissues by LC-MS approach (Fig. 4, A and B). We observed

significant changes in purine and pyrimidine metabolism in both steatotic and NASH livers relative to controls (Fig. 4, C and D). Overall, our data demonstrate that nucleotide pool imbalance is a key feature of NAFLD and contributes to replication stress in steatotic hepatocytes.

Replicating NAFLD hepatocytes display cGAS-STING pathway activation.

We finally investigated whether DNA lesions induced by replication stress in NAFLD hepatocyte could be sensed by components of the innate immune system. A recent study has demonstrated in cancer cell lines a connection between replication stress and the cytosolic DNA sensing pathway (also named cyclic GMP-AMP synthase – stimulator of interferon genes or cGAS-STING pathway) (Coquel et al., 2018). This pathway is involved in various biological processes, including type I interferon (IFN-I) production, senescence and inflammation (Li and Chen, 2018). First, by using RNAscope technology, we found an *in vivo* upregulation of *Sting* expression in HFHS and CDHFD livers compared to SD (Fig. 5 A). Interestingly, we also found in our transcriptome analysis of replicating hepatocytes an upregulation of pathways related to cGAS/STING such as the "Cytosolic DNA sensing pathway" and inflammatory/immune pathways (Fig. 5 B). To better understand this mechanism, we first investigate the source of cytosolic DNA that could activate cGAS/STING signaling. We quantified micronuclei in proliferating SD and NAFLD hepatocytes and observed no specific accumulation in HFHS, CDHFD hepatocytes compared to SD (Fig. S5 A). Leak of ssDNA fragments was quantified by measuring the Histone H3 into cytoplasmic extracts (Parkes et al., 2017). We found a drastic increased of Histone H3 into the cytosolic compartment of proliferating NAFLD hepatocytes (HFHS, CDHFD) but not in normal hepatocytes (SD) (Fig. S5 B). We next characterized cGAS activation by

measuring the production of the second messenger cyclic GMP-AMP (cGAMP). LC-MS results showed a specific production of cGAMP in NAFLD hepatocytes harboring replication stress (60 h vs. 36 h; Fig. 5 C). In correlation, molecular analysis also highlighted about an increase of STING expression at the mRNA and protein level (Fig. S5 C, Fig 5 D and E). The levels of *Ifn-β* and IFN-stimulated gene (ISGs: *Mx1* and *Isg15*) transcripts were also higher in these cells (Fig. S5 D). Most importantly, quantification of IFN-β synthesis revealed that this cytokine was overproduced in NAFLD hepatocytes that had experienced replication stress (60 h vs. 36 h; Fig. 5 F and G). Together, these data strongly suggest that the replication stress observed in NAFLD hepatocytes drives activation of the cGAS-STING pathway. We tested this hypothesis by determining whether dNTP supplementation during replication stress could modulate activation of the DNA-sensing pathway. We found that the addition of dNTPs reduces activation of the DNA sensing pathway, with a decrease of cGAMP production, STING expression and IFN-β production (Fig. 5, H, I, J and K). Finally, we investigated the relationship between hepatic *cGAS* and *STING* expression and human NAFLD progression. Human liver biopsy specimens from morbidly obese patients (n=27) were selected and classified into two groups: with and without NAFLD (Table 2). We observed that the levels of *cGAS* and *STING* mRNA in the liver were upregulated specifically in obese patients with NAFLD (Fig. 5 L and M), and levels of *cGAS* and *STING* expression were positively correlated with each other (Fig. 5 N). *STING* expression was also positively correlated with NAFLD activity score (NAS) (Fig. 5 O). Together, these data show that replication stress in NAFLD hepatocytes drives activation of the DNA-sensing pathway. They also suggest a role for DNA-sensing pathway in human NAFLD progression.

Discussion

Non-alcoholic steatotic liver disease is complex, and its pathogenesis has not been yet clearly elucidated. Steatohepatitis (NASH) causes more liver damage than simple steatosis (NAFL). Considerable efforts are therefore being made to find ways of stopping the chain of events driving the NAFL/NASH sequence. Here, we demonstrate, for the first time, that NAFLD hepatocytes display hallmarks of replication stress, including slow replication fork progression and the activation of an S-phase checkpoint (ATR signalling). Replication-associated DNA lesions accumulate in NAFLD hepatocytes, and the nucleotide pool imbalance occurring during NAFLD is the key driver of replication stress. Finally, we show that NAFLD hepatocytes that have experienced replication stress display an activation of the cGAS-STING pathway, inducing a type I interferon response. Overall, our data shed new light on the mechanisms by which damaged steatotic hepatocytes might promote NASH progression.

Recent studies have provided evidence for a role of the gradual accumulation of DNA lesions in NAFLD progression (Anstee et al., 2019). Thus, accumulation of oxidative DNA damage has been shown to be associated with the worsening of human NAFLD (Nishida et al., 2016; Pinyol et al., 2021; Tanaka et al., 2013). Consistently, a reduction in nucleotide excision repair (NER) is observed during the human steatosis/NASH sequence related to hepatic inflammation (Schults et al., 2012). In fact, in various chronic liver diseases, DNA damage and genetic instability are hallmarks of disease aggravation enhanced by compensatory regeneration (Anstee et al., 2019; Boege et al., 2017). Our study demonstrate that DNA damage can also be induced by replication stress in steatotic hepatocytes. First, we show a decrease in replication fork speed in proliferating NAFLD hepatocytes, reflecting the replication stress suffered by these

cells. We also brought the clues that replication stress was sufficient to elicit DNA lesions. Interestingly, our findings highlighted some differences between the two NAFLD mice model used. Of note, the NAFLD activity score was significantly higher in CDHFD livers due to the presence of a marked steatosis and the presence of lobular inflammation. Comparing accumulation of DNA lesions, we showed that HFHS hepatocytes present simple DNA lesions (comet tail without 53BP1 foci) while CDHFD hepatocytes present in addition double-strand breaks DNA lesions (comet tail with 53BP1 foci). Our dNTPs supplementation experiments reinforced the idea about the different nature of these lesions. In fact, our data suggest that, in proliferating CDHFD hepatocytes, dNTPs supplementation is mainly used for repair mechanisms limiting DNA replication rate. Proliferating CDHFD hepatocyte also presented a weaker activation of the ATR pathway (pCHK1 and pRPA) compared to HFHS, favoring the hypothesis for an underperforming ATR-mediated signaling in CDHFD hepatocytes. One function of ATR is to cope with stalled DNA replication forks in order to avoid fork collapsing and DSB occurrence (López-Contreras and Fernandez-Capetillo, 2010). Interestingly, we previously reported that fibroblasts from a patient carrying compound heterozygous variants in the ATR gene, causing a reduced ATR-dependent DNA damage signaling, exhibited DSB accumulation (Mokrani-Benhelli et al., 2013). We can suggest that during NAFL/NASH sequence, replication stress conjointly to an underperforming DDR could drive accumulation of more severe DNA lesions in steatotic hepatocytes and may favor transformation.

Replication stress is a major driver in the development and progression of many cancers and more recently has been shown to be involved in diseases related to autoimmunity and chronic inflammation (Orvain et al., 2020; Ragu et al., 2020; Schild-Poulter et al., 2008; Toledo et al., 2013). Our data show that in NAFLD, an emblematic

metabolic reprograming disease, fat overload in hepatocytes drives replication stress. The sources of replication stress can be diverse (Magdalou et al., 2014; Zeman and Cimprich, 2014). The size and balance of the dNTP pools are major determinants of fork speed and genome stability (Techer et al., 2017). Various studies have shown that nucleotide pool disequilibrium in precancerous and cancerous human cells impedes fork progression, leading to genome instability (Bester et al., 2011; Chabosseau et al., 2011). We now show that a nucleotide pool imbalance promotes replication stress in the context of NAFLD. Indeed, one of the key findings of our study was that nucleoside supplementation was partially sufficient to prevent the activation of the S-phase checkpoint and the accumulation of DNA damage/breaks. This finding suggested that DNA replication proceeds under suboptimal conditions during NAFLD progression. Our metabolomic analyses also revealed both in murine and human NAFLD livers an alteration in purine and pyrimidine metabolism. Both purine and pyrimidine production involve multiple metabolic pathways, which can be differentially affected by nutrient and/or redox perturbations (Zhu and Thompson, 2019). Importantly, we demonstrated that oleic and palmitic fatty acids overload in proliferating ΔHepaRG was sufficient to provoke a disbalance in purine and pyrimidine pathways. Further studies are required to identify factors affecting this dysregulation. Studying metabolism at single-cell resolution seems to be the best options to correlate DNA lesions accumulation in proliferating NAFLD hepatocytes with metabolism reprogramming.

Another important finding of this study is the link we have established between DNA lesions induced by replication stress in NAFLD hepatocytes and activation of the cGAS-STING pathway. This cytosolic DNA sensor was initially identified as playing a key role in the generation of an immune response to DNA viruses and bacteria (Li and Chen, 2018; Schoggins et al., 2014; Tan et al., 2018). Several studies have since

demonstrated that the cGAS-STING pathway is activated by DNA damage in antitumor immunity, senescence, apoptosis and inflammatory responses (Li and Chen, 2018; Ragu et al., 2020). cGAS senses cytoplasmic DNA resulting from nuclear DNA damage. This nuclear DNA damage may generate either micronuclei due to chromosome mis-segregation or a cytosolic accumulation of replication fork-derived single-stranded DNA (ssDNA) related to replication stress (Coquel et al., 2018; Li and Chen, 2018; Ragu et al., 2020; Schoggins et al., 2014; Tan et al., 2018). By contrast to what has been previously reported (Luo et al., 2018; Yu et al., 2019), we observed that normal hepatocytes do express *Sting*, weakly, at the mRNA level. In the context of NAFLD, we demonstrated that macrophages are not the only contingent of cells capable of activating the cGAS-STING pathway (Luo et al., 2018; Wang et al., 2020). Indeed, *Sting* expression was enhanced in nonalcoholic steatotic hepatocytes. More importantly, our findings demonstrate that the cGAS-STING pathway connects hepatocyte replication stress to interferon production in NAFLD. Recent studies have provided evidence to suggest that exonucleases are essential for ssDNA degradation in cancer cells, and for restraining the cGAS-STING response (Coquel et al., 2018; Yang et al., 2007). It could be speculated that exonuclease activity is downregulated during NAFLD. Given the role of the cytosolic DNA-sensing cGAS-STING pathway in activating immune surveillance, it has generally been assumed that this pathway has a primary tumor suppressor function (Li and Chen, 2018; Ragu et al., 2020; Yu et al., 2015). However, there is growing evidence to suggest that, depending on the context, this pathway can also drive inflammation-mediated tumorigenesis (Ahn et al., 2014; Kwon and Bakhoum, 2020; Li and Chen, 2018). Future studies are required to determine whether replication stress and the cGAS-STING pathway may prevent or drive NAFLD-associated HCC development.

Acknowledgments

The authors are grateful to Pierre Henri Gaillard and Géraldine Gentric for their critical evaluation of the work and to all members of the laboratory for fruitful discussions. We thank the Tumor Biobank of Henri Mondor University Hospital and the Réseau National Centre de Ressources Biologiques (CRB) Foie for contributing to the tissue collection. We thank the functional experimentation center of La Pitié-Salpêtrière as well as the Core facilities of the Centre de Recherche des Cordeliers: CHIC (Center of Histology Imaging and Cytometry), CGB (Genotyping and biochemical Center) and CEF (Functional Exploration Center). We thank also Genomic facility (GENOM'IC) (Institut Cochin, INSERM U1016, Paris, France) and Platform for Metabolic Analyses (SFR Necker, INSERM US24/CNRS UMS 3633, Paris, France). We finally thank the Montpellier DNA Combing platform for their contribution to the DNA combing experiments.

Authors contribution

R.D, M.S.A, P.C, A.H, M.S., C.K, T.R, I.G.F, Mo.H, M.D.C, I.N, S.C, S.B, R.Ö, V.P, P.R, and C.D performed and analyzed experiments involving mouse experiments, human cohorts studies, primary hepatocytes cultures, metabolically competent human hepatocyte-like cell cultures, gene expression analyses, DNA combing, LC-MS, imaging, qRT-PCR, and molecular/cellular techniques. R.D performed mouse experiments, primary hepatocyte cultures, gene expression analyses, DNA combing, LC-MS analyses, imaging, qRT-PCR, and molecular/cellular techniques. M.S.A, P.C, A.H, C.K, I.G.F performed mouse experiments, molecular/cellular techniques and imaging. Mo.H, M.D.C and P.R performed DNA combing. M.S and T.R performed metabolically competent human hepatocyte-like cell cultures. I.N performed LC-MS.

S.C performed GSEA analysis. M.S, R.Ö, R.R and K.U performed RNAseq experiment and analysis of the pathways. S.B performed qRT-PCR of the human cohort. R.D, M.S.A, P.C, A.H, M.S, I.N, A.T, P.G, JP.C, V.P, S.CM., M.H, P.R, C.D analyzed and interpreted experimental data. R.D and C.D wrote the manuscript. R.D and C.D conceived and designed the study. All authors commented on the manuscript. All data needed to evaluate the conclusions in the paper are presented in the paper or the Supplemental Information and STAR METHODS.

Financial support

The authors are supported by French grants from the Institut National de la Santé et de la Recherche Médicale (INSERM), la Fondation pour la Recherche Médicale (Equipe FRM: EQU201903007824), the Institut National du Cancer (PRTK-2017, PLBIO18-107), the Agence Nationale de Recherche ANR (ANR-16-CE14 ; ANR-19-CE14-0044-01), Fondation ARC (Association de Recherche sur le Cancer), Ligue Contre le Cancer (comité de Paris), the Cancéropôle Ile-de-France (Emergence 2015), The Association Française pour l'Etude du Foie (AFEF-SUBV 2017 ; AFEF-SUBV 2019), EVA-Plan Cancer INSERM HTE and the SIRIC CARPEM. R.D. was a recipient of Ministère de la Recherche and Fondation pour la Recherche Médicale (PhD grant) and supported by the EUR G.E.N.E. (reference #ANR-17-EURE-0013) and is part of the Université de Paris IdEx #ANR-18-IDEX-0001 funded by the French Government through its "Investments for the Future" program. P.C. is a recipient of Plan Cancer INSERM (program « Soutien pour la formation à la recherche fondamentale et translationnelle en cancérologie »).

Legend of figures

Figure 1 | NAFLD hepatocytes experience replication stress. (A) Experimental procedure. **(B)** (Top) DNA combing method. Dual-pulse labeling (CldU and then IdU, 30 min each) was performed between 47 and 48 hours of culture. (Bottom) Representative images of the DNA combing experiment (magnification, x40). **(C)** Quantification of replication fork speed in three independent experiments, with 150 fibers analyzed per experiment. One-way ANOVA with Tukey's test for multiple comparisons. **(D)** Immunoblot analysis of the phosphorylation of $CHK1^{s317}$ and $RPA32^{s33,}$ in primary hepatocyte cultures at 60 hours. HSC70 was used as a loading control. **(E)** Quantification of the levels of p-$CHK1^{s317}$ and p-$RPA32^{s33}$ normalized on HSC70. One-way ANOVA with two-stage comparisons method. (n=3 per group) **(F)** Gene set enrichment analysis (GSEA), at 48 hours of culture for proliferating HFHS and CDHFD hepatocytes (normalized against SD with enrichment score [ES] >1.25 (red bars), n=3 *ex vivo* cultures per group). The p-value was generated by the software. **(G)** Heat-map showing the enrichment of genes involved in DNA replication and DNA repair in HFHS/CDHFD compared to SD proliferating hepatocytes, extracted from transcriptomic analysis. **(H)** Relative transcript levels (determined by RT-qPCR) for genes involved in different DNA repair and DNA lesion signaling in proliferating SD, HFHS and CDHFD hepatocytes, at 48 hours. The data shown are the mean ± SEM (n=8 per group). Blue and red asterisks represent comparisons between HFHS and SD and between CDHFD and SD, respectively. One-way ANOVA with Tukey's test for multiple comparisons.

Figure 2 | Replication-associated DNA lesions accumulate in proliferating

NAFLD hepatocytes. (A) Immunofluorescence staining for γH2AX (green) and PCNA (red) with Hoechst counterstaining on liver tissue sections (representative images). Original magnification, ×40. The white bar indicates 20 µm. (*n*= 7 SD; 9 HFHS and 8 CDHFD) **(B)** Histogram representing all the PCNA positive cells, positive or not for γH2AX marker. The PCNA-γH2AX double-positive hepatocytes indicates damaged proliferative hepatocytes. One-way ANOVA with Tukey's tests for multiple comparisons for each time point. **(C)** Immunoblot analysis comparing H2AX phosphorylation on the serine 139 residue (γH2AX) in hepatocyte cultures at 36 and 60 hours. HSC70 was used as a loading control. (*n*= 3 SD; 4 HFHS and 4 CDHFD) **(D)** Quantification of γH2AX at 36 and 60 hours. The data shown are the mean ± SEM. One-way ANOVA with Tukey's test for multiple comparisons at each time point. **(E)** Immunofluorescence staining for γH2AX (green) and pHH3 (red) with Hoechst counterstaining in hepatocytes at 60 hours of culture (representative images). Original magnification, ×20. The white bar indicates 20 µm. White arrowheads indicate double positive nuclei **(F)** Quantification of γH2AX staining intensity according to the absence (pHH3-) or presence (pHH3+) of the pHH3 G2/M marker in proliferating NAFLD hepatocytes at 60 hours. Unpaired two-tailed *t*-test, with the mean and quartiles shown as solid and dashed lines, respectively (*n*=3 per group). (*n*= 4 SD; 4 HFHS and 4 CDHFD) **(G)** Left panel: Representative COMET images of nuclei pretreated with alkaline solution and subjected to electrophoresis. Original magnification, ×10. The white bar indicates 20 µm. Right panel: Quantification of the comet tail length (*n*=3 experiments per group, at least 170 nuclei were analyzed per experiment and per group). The results are presented as the mean ± SEM. Kruskal-Wallis test with Dunn's test for multiple comparisons. **(H)** Immunofluorescence staining of 53BP1 with Hoechst counterstaining in SD, HFHS, CDHFD hepatocytes at 60 hours of culture

(representative images). Arrowheads mark 53BP1 nuclear foci. Original magnification, ×20. The white bar indicates 20 µm. (*n*=3 experiments per group at least 150 nuclei were analyzed per experiment and per group) **(I)** Quantification of 53BP1 foci distribution (<4 and ≥4) in SD, HFHS, CDHFD hepatocytes. Two-way ANOVA test.

Figure 3 | Replication stress in NAFLD hepatocytes is induced by nucleotide pool imbalance. **(A, B)** Enrichment map representing fold enrichments and *p*-values for pathways deregulated in HFHS **(A)** and CDHFD **(B)** livers compared to SD livers. Metabolite set enrichment analysis was determined by LC-MS (*n*=4 SD, 5 HFHS and 5 CDHFD). **(C)** Heat map showing relative levels of metabolites involved in purine and pyrimidine metabolism. Data were extracted from LC-MS metabolite quantification. **(D)** Relative levels of dNTPs (dATP, dTTP, dGTP and dCTP, respectively) measured by LC-MS, at 48h of culture. The results are presented as the mean ± SEM. For each dNTP, one-way ANOVA was performed with Tukey's test for multiple comparisons. **(E)** DNA combing analysis during the rescue experiment. Quantification of replication fork speed in two independent experiments for each model in each condition (+/- dNTPs), with at least 100 fibers analyzed per experiment. Mann-Whitney T-test was used to compared each experiment. **(F-I)** Representative immunoblot analysis comparing the phosphorylation of CHK1 (S317) **(F)** and H2AX (S139) **(H)** in hepatocyte cultures during the dNTPs rescue experiment. For each experiment, 20 µM of dATP, dCTP, dGTP and thymidine was added at 36 h and 48 h of culture. Proteins were extracted at 60 hours of culture. HSC70 were used as a loading control (*n*=4 SD, 6 HFHS and 7 CDHFD). Quantification of γH2AX **(G)** and pCHK1 **(I)** was normalized to HSC70 for each hepatocyte culture. The data shown are the mean ± SEM. Unpaired two-tailed *t*-test.

Figure 4 | Human NAFLD livers display alterations to purine and pyrimidine metabolism. (A) PCA plot representing clustering of samples from Healthy, Steatotic and NASH liver tissues used for metabolomic analysis, performed with the Metaboanalyst software. The cohort is described in Table 1. **(B)** Clustered heat map showing the 50 most dysregulated metabolites, measured by LC-MS and analyzed with the metaboanalyst software. **(C/D)** Enrichment maps showing fold enrichment and *p*-values for the metabolic pathways deregulated in the livers of patients with steatosis **(A)** and NASH **(B)** relative to control patients. Metabolite set enrichment analysis for the LC-MS experiment was performed with the Metaboanalyst website.

Figure 5 | Replication stress promotes cGAS/STING pathway activation in NAFLD hepatocytes. (A) (Left panel) *In situ* hybridization (RNAscope®) directed against *Sting* mRNA in SD, HFHS and CDHFD livers. The white bar indicates 20 µm. (Right panel) Quantification of the number of dots per hepatocyte only. Two-way ANOVA test. (*n*=3 animals per group, 500 hepatocytes per animal were analyzed in different lobes). **(B)** GSEA showing the upregulated pathways, which are involved in DNA sensing and inflammatory/immune pathways, at 60 hours of culture (normalized against SD with an enrichment score [ES] <-1.3 (red bars), *n*=3 animals per group). The *p*-value was determined with the GSEA program. **(C)** cGAMP production measured by LC-MS at 36h and 60h. The data shown are the mean ± SEM. One-way ANOVA with Tukey's test for multiple comparisons at each time point. **(D)** Immunoblot analysis comparing the expression of STING at 36 h and 60 h of culture. HSC70 was used as a loading control. **(E)** Quantification of STING levels normalized against HSC70. One-way ANOVA with Tukey tests. **(F)** Quantification of IFN-β protein in

STAR METHODS

KEY RESOURCES TABLE

REAGENT or RESOURCE	SOURCE	IDENTIFIER
ANTIBODIES		
α-53BP1 (Immunostaining)	Novus	Cat# NB100-304; RRID: AB_10003037
α-pCHK1^{S317}(Immunoblotting)	Cell Signaling Technology	Cat#12302 ; RRID: AB_2783865
α-CldU (rat anti-BrdU) clone BU1/75-ICR (DNA combing)	Abcam	Cat# Ab6326; RRID: AB_305426
α-γH2AX^{S139} (Immunostaining)	Merck-Millipore	Cat# 05-636; RRID: AB_309864
α-γH2AX^{S139} (Immunoblotting)	Cell Signaling Technology	Cat# 9718; RRID: AB_2118009
α-γ-tubulin (Immunoblotting)	Merck	Cat# T5326; RRID: AB_532292
α-HSC-70 (Immunoblotting)	Santa Cruz Biotechnology	Cat# 7298; RRID: AB_627761
α-IdU (mouse anti-BrdU) (DNA combing)	BD Biosciences	Cat# 347580; RRID: AB_10015219
α-pHH3 (Immunostaining)	Merck	Cat# 06-570; RRID: AB_310177
α-pRPA^{S33} (Immunoblotting)	Béthyl	Cat# A300-246A; RRID: AB_2180847
α-ssDNA antibody (DNA combing)	Merck	Cat# MAB3034; RRID: AB_94645
α-STING (Immunoblotting)	Cell Signaling Technology	Cat# 13647; RRID: AB_2732796
α-Mouse IgG (Immunoblotting)	Cell Signaling Technology	Cat# 7076; RRID: AB_330924
α-Rabbit IgG (Immunoblotting)	Cell Signaling Technology	Cat# 7074; RRID: AB_2099233
α-Goat anti-mouse Alexa Fluor 488 (Immunostaining)	Thermo Fisher Scientific	Cat# A11001; RRID: AB_2534069
α-Goat anti-mouse Alexa fluor 594 (Immunostaining)	Thermo Fisher Scientific	Cat# A11005; RRID: AB_141372
α-Goat anti-rabbit Alexa Fluor 488 (Immunostaining)	Thermo Fisher Scientific	Cat# A11008; RRID: AB_143165
α-Goat anti-rabbit Alexa Fluor 594 (Immunostaining)	Thermo Fisher Scientific	Cat# A11012; RRID: AB_141359
α-rat Cy5 (DNA combing)	Abcam	Cat# Ab6565; RRID: AB_955063
α-anti mouse Cy3.5 (DNA combing)	Abcam	Cat# Ab6946; RRID: AB_955045

Chemicals, Peptides, and Recombinant Proteins		
BSA (Bovine Serum Albumin)	Merck	Cat#A9576; CAS: 9048-46-8
5-Chloro-2-deoxyuridine (CldU)	Merck	Cat#C6891; CAS: 50-90-8
2′-Deoxyadenosine monohydrate (dATP)	Merck	Cat#D8668; CAS: 16373-93-6
2′-Deoxycytidine hydrochloride (dCTP)	Merck	Cat#D0776; CAS: 3992-42-5
2′-Deoxyguanosine monohydrate (dGTP)	Merck	Cat#D7145; CAS: 312693-72-4
DMSO (DiMethylSulfOegfxide) Hybrid-MaxTM	Merck	Cat#D2650
EGF (Epidermal Growth Factor)	Merck	Cat#E4127; CAS: 62229-50-9
Hoechst 33342, Trihydrochloride, Trihydrate	Thermo Fisher Scientific	Cat#H3570; CAS: 23491-52-3
Insulin solution from bovine pancreas	Merck	Cat#I0516
Human insulin	Merck	Cat#I9278
Hydrocortisone hemisuccinate	Merck	Cat#1319002; CAS: 83784-20-7
5-Iodo-2-deoxyuridine (IdU)	Merck	Cat#I7125; CAS: 54-42-2
Oil Red O	Merck	Cat#O0625 ; CAS : 1320-06-5
Proteinase K Solution RNA Grade 20 mg	Thermo Fisher Scientific	Cat#100005393; CAS: 39450-01-6
Pyruvate Sodium	Merck	Cat#P4562; CAS: 113-24-6
Sodium oleate	Merck	Cat#O3880; CAS: 143-19-1
Sodium palmitate	Merck	Cat#P9767; CAS: 408-35-5
Thymidine	Merck	Cat#T1895; CAS: 50-89-5
Recombinant Mouse TNF-α (aa 80-235)	R&D systems	Cat#410-MT
Recombinant Human TNF-α	R&D systems	Cat#210-TA
Critical Commercial Assays		
β-Glycerophosphate, Disodium Salt, Pentahydrate	Merck	Cat#35675; CAS: 13408-09-8

5-Bromo-2-deoxy-uridine Labeling and Detection Kit I	Merck	Cat#11296736001
Choline-Deficient High-Fat Diet	Research Diets	Cat#D05010402i
High-Capacity cDNA Reverse Transcription Kit	Thermo Fisher Scientific	Cat#4368813
High-Fat High-Sucrose	Safe	Cat#U8954P Version 014
Mouse IFN-beta DuoSet ELISA	R&D systems	Cat# DY8234-05 and DY008
NE-PER Kit	Thermo Fisher Scientific	Cat# 78833
OxiSelect™ Comet Assay Kit	Cell Biolabs	Cat#STA-351
Pierce™ BCA Protein Assay Kit	Thermo Fisher Scientific	Cat#23225
Pierce™ Protease Inhibitor Tablets	Thermo Fisher Scientific	Cat#A32965
RIPA	Merck	Cat#R0278
Standard Diet	Safe	Cat#R04-10
SYBR Luminaris Color HiGreen qPCR master mix	Thermo Fisher Scientific	Cat#K0394
TRIzol™ Reagent	Thermo Fisher Scientific	Cat#15596018
Deposited Data		
Transcriptomic data	GEO	GSE154194
Experimental Models: Cell Lines		
HepaRG	DKFZ, Division of Chronic Inflammation and Cancer	NA
Experimental Models: Organisms/Strains		
Mouse (Male): C57BL/6J	Janvier Laboratories	C57BL/6JRj
Oligonucleotides		
Mouse 18S Forward	5'-GTAACCCGTTGAACCCCATT	This paper
Mouse 18S Reverse	5'- CCATCCAATCGGTAGTAGCG	This paper
Mouse Brca1 Forward	5'-TCCACAGTTCAAAAGCACC	This paper
Mouse Brca1 Reverse	5'-TCTTTGTTTCTTCACTGCTACC	This paper
Mouse Cyclin A2 Forward	5'- GCCTTCACCATTCATGTGGAT	This paper
Mouse Cyclin A2 Reverse	5'- TTGCTCCGGGTAAAGAGACAG	This paper
Mouse Ercc1 Forward	5'-CCACAACCTCCATCCAGACT	This paper
Mouse Ercc1 Reverse	5'-CCTGCTGGGGATCTTTCA	This paper

Mouse Fancl Forward	5'-CTTTCTAAAATGACAAACCAGCAC	This paper
Mouse Fancl Reverse	5'-TGTCTGATCATCTCGTGGATTT	This paper
Mouse Gadd45a Forward	5'-AGAGCAGAAGACCGAAAGGA	This paper
Mouse Gadd45a Reverse	5'-CGTAATGGTGCGCTGACTC	This paper
Mouse Ho1 Forward	5'-AAGCCGAGAATGCTGAGTTC	This paper
Mouse Ho1 Reverse	5'- GCCGTGTAATATGGTACAAGGA	This paper
Mouse Hqo1 Forward	5'- AGCGTTCGGTATTACGATCC	This paper
Mouse Hqo1 Reverse	5'- AGTACAATCAGGGCTCTTCTGG	This paper
Mouse Ifnβ Forward	5'-GCACTGGGTGGAATGAGACT	This paper
Mouse Ifnβ Reverse	5'-AGTGGAGAGCAGTTGAGGACA	This paper
Mouse Isg15 Forward	5'- CAGGACGGTCTTACCCTTTCC	This paper
Mouse Isg15 Reverse	5'- AGGCTCGCTGCAGTTCTGTAC	This paper
Mouse Mx1 Forward	5'- GATCCGACTTCACTTCCAGATGG	This paper
Mouse Mx1 Reverse	5'- CATCTCAGTGGTAGTCAACCC	This paper
Mouse Neil Forward	5'-CGCCCATCTACGTTTTTACAC	This paper
Mouse Neil Reverse	5'-TCTACGAAGCAAAGGGCAAG	This paper
Mouse Ogg1 Forward	5'-CCTTATGAAGAGGCCCACAA	This paper
Mouse Ogg1 Reverse	5'-GTCAAGGGCCATTAAGCAGA	This paper
Mouse Rad51 Forward	5'-CGAGGGTTCAACACAGACC	This paper
Mouse Rad51 Reverse	5'-CTGTCTACAATAAGCAGTGCATACC	This paper
Mouse Xpc Forward	5'-GATGATGAAGCGTTTCAATAAAGA	This paper
Mouse Xpc Reverse	5'-GATGCTATTTCGATAGAAGCCACT	This paper
Mouse Xpf Forward	5'-GCAGAAAATAAGGAGAGCGAAG	This paper
Mouse Xpf Reverse	5'-ATCGCTTGCACAGATCAGC	This paper
Software and Algorithms		
Graphpad Prism 7	Graphpad	https://www.graphpad.com/scientific-software/prism/
ImageJ - J 1.8.0_112	ImageJ	https://imagej.net/Welcome
Heatmapper	Heatmapper	http://www.heatmapper.ca/expression/
Metaboanalyst 4.0	Metaboanalyst	https://www.metaboanalyst.ca/
Open Comet: Image J tool	(Gyori et al., 2014)	http://www.cometbio.org/

R	The R Project for Statistical Computing	https://www.r-project.org/

RESOURCE AVAILABILITY

Lead contact

Further information and requests for reagent and resources should be addressed to the lead contact, Chantal Desdouets (chantal.desdouets@inserm.fr) or the first author Romain Donne (romain.donne@inserm.fr).

Data and code availability

RNA-seq data regarding HepaRG experiments are the property of Mathias Heikenwalder's lab and will be deposed soon in GEO.

EXPERIMENTAL MODEL AND SUBJECT DETAILS

Human Material

For transcriptomic analysis: Twenty-seven morbidly obese patients were recruited through the Department of Digestive Surgery and Liver Transplantation (Nice hospital, France) and where they underwent bariatric surgery for their morbid obesity **(Table 2)** in accordance with French guidelines. Exclusion criteria were: presence of a hepatitis B virus or hepatitis C virus infection, excessive alcohol consumption (>20g/day) or another cause of chronic liver disease as described (Patouraux et al., 2017). Before surgery, fasting blood samples were obtained and used to measure alanine and aspartate transaminases (ALT and AST, respectively), glucose, insulin and HbA1c. Insulin resistance was calculated using the homeostatic model assessment (HOMA-IR) index. Surgical liver biopsies were obtained during surgery and no ischemic preconditioning had been performed. Hepatic histopathological analysis was performed according to the scoring system of Kleiner et al. (Kleiner et al., 2005).

For metabolomics analysis: Eight NAFLD patients were recruited through the Department of Digestive Surgery and Hepatology (Beaujon hospital, France); where they underwent resection for HCC (Table 1). Exclusion criteria were same as Nice Hospital. For each patient a SAF score (steatosis, activity, fibrosis) summarizing the main histological lesions was defined (Bedossa et al., 2012). Also, the NAS score was attributed according to Kleiner et al. (Kleiner et al., 2005). Control patients (n=5) underwent liver resection for benign tumors. All subjects gave their informed written consent to participate in this study in accordance with French legislation regarding Ethics and Human Research (Huriet-Serusclat law). The "Comité Consultatif de Protection des Personnes dans la Recherche Biomédicale de Nice" approved the study (07/04:2003, N° 03.017) and Assistance Publique - Hôpitaux de Paris (DC-2009-936)

Mice models

C57BL/6J lean male mice were purchased from Janvier Laboratories at 4 weeks of life and housed in a temperature-controlled environment with 12-hour-light/dark cycles. All animals had free access to water and standard diet (**SD**) (R04-10, Safe), providing 60% carbohydrate, 3% fat and 16% protein in terms of energy. After one week, 5-week-old C57BL/6J mice were assigned randomly to 3 groups fed for 6 months with SD or High-Fat High-Sucrose diet (**HFHS**) (U8954P Version 014, Safe), providing 50% carbohydrate, 23% fat, and 17% protein in terms of energy, or a Choline–Deficient High-Fat Diet (**CDHFD**) (D05010402i, Research Diets), providing 42% carbohydrate, 24% fat, and 24% protein without choline. Body weight was monitored monthly. For *in vivo* experiments, animals were humanely euthanized and livers were harvested. One part of the liver was fixed in phosphate-buffered 10% formalin for histological analyses

and the remaining tissue was immediately frozen in liquid nitrogen and stored at –80°C until processing. The NAS score was evaluated according to the scoring system of Kleiner et al. (Kleiner et al., 2005). Mice received care in compliance with institutional guidelines regulated by "Direction départementale de la protection des populations", France (authorization number 13996).

Cell isolation and culture of murine primary hepatocytes

Hepatocytes were isolated from mouse livers by *in situ* perfusion and were seeded in complete medium, as described previously (Fortier et al., 2017). Hepatocytes were isolated from 7-month-old SD or NAFLD mice (HFHS or CDHFD, following 6 months of diet). Cell viability after liver perfusion was equivalent (≥80%) in all mouse models. After cell spreading, the culture medium (William's #32551087) was deprived of fetal bovine serum. Proliferation (S phase synchronization) was induced with 50 ng/mL mitogenic EGF (Merck #E4127) and 20 mM of pyruvate sodium (Merck #P4562). For rescue experiments, 20 µM of each dNTPs/nucleotide (dATP, dCTP, dGTP and Thymidine) was added. dCTP (Merck D0776) was solubilized in 1 M NaOH (100 mM). dATP (Merck D8668) was solubilized in 0.1 M NaOH (20 mM). Thymidine (Merck T1895) was solubilized in H2O (50 mM). dGTP (Merck D7145) was solubilized in 1 M NH4OH (100 mM). Half of the primary culture was treated twice with 20 µM of the nucleotide mixture at 36h and 48h of culture time. The other half was treated with the same amount of resuspension buffer without nucleotides. Incorporation of the thymidine analogue (BrdU; Merck #11296736001) was used as an index of replication between 48h and 60h.

HepaRG culture and in vitro fatty acid uptake

HepaRG human (Biopredic, Rennes, France) were cultured at 37°C and 5% CO_2 in a humidified incubator. HepaRG were differentiated with DMSO (Merck #D2650) and cultivated, as described previously (Gripon et al., 2002), including a 2 week incubation with 10% fetal bovine serum, 5µg/mL of human insulin (Merck # I9278), 5×10^{-7} M hydrocortisone hemisuccinate (Merck #1319002) and 1.8% dimethyl sulfoxide (DMSO; Merck #D2650) for the induction of differentiation into hepatocyte-like cells (ΔHepaRG). When cells were confluent, medium was changed with only 2% fetal bovine serum, and cells were treated during 4 days with fatty acids (66 µM of sodium oleate (Merck #O3880) and 33 µM of sodium palmitate (Merck P9767)). RNAseq analysis was performed after 24h of FA treatment. Then, cells were trypsinized and plated (300 000 cells per well in 6-wells plate) to induce proliferation. Experiments were performed 48 hours later. To assess intracellular neutral lipid, HepaRG cells were fixed using 4% paraformaldehyde during 20 minutes and stained using Oil-Red-O solution (Merck # O0625) for 25 minutes at room temperature, followed by Hoechst staining during 10 minutes. Lipid accumulation was quantified using Image J. The quantified area of Oil Red O staining was reported to the cell number thanks to Hoechst staining.

DNA combing

Primary cultures were sequentially labeled with 25 µM of CldU (Merck #C6891) and then 25 µM of IdU (Merck #I7125) for 30 minutes, each, as previously described (Lebofsky and Bensimon, 2005). For the rescue analysis, CldU/IdU were added to the dNTPs mixture without thymidine. Cells were harvested and embedded in low-melting agarose plugs (from Comet assay kit) in which DNA was subjected to deproteinization by proteinase K treatment (ThermoFisher Scientific #100005393). Agarose was then removed by digestion with agarase and the high molecular DNA yielded was used for

combing as previously described (Michalet et al., 1997) by using the FiberComb® Molecular Combing System (Genomic Vision). CldU and IdU was respectively stained with rat anti-BrdU and mouse anti-BrdU antibodies, followed by staining with anti-rat Cy5 and anti-mouse Cy3.5 (See Supplementary Table 2). DNA fibers were counterstained with anti-ssDNA antibodies to distinguish fork pausing/stalling from fiber breakage. DNA fibers were visualized using the FiberVision® scanner (Genomic Vision). Data analysis was performed as described (Rimmele et al., 2010).

Comet assay

The Comet assay was performed by using the Oxiselect STA-351 kit (Cell Biolabs #STA-351). Individual hepatocytes were mixed with molten agarose before application to the OxiSelectTM Comet Slide. Embedded cells were treated with the lysis buffer during 1 hour at 4°C and then treated with the alkaline solution during 30 minutes at 4°C. Finally, slides were electrophoresed in a horizontal chamber during 30 minutes in the alkaline solution at 300 mA and 25 volts. DNA was then stained with the DNA dye and visualized by epifluorescence microscopy. Quantification was performed by using the "OpenComet" open-source software tool (Gyori et al., 2014) for Image J, and by following the published instruction. Images were taken using a Nikon Statif Eclipse E600 microscope with x10 magnification, a DXM1200 cooled CCD camera (Nikon), and ACT-1 (version 2.63; Universal Imaging).

Metabolomic analyses by LC-MS

Metabolomic analyses were performed as previously described by Liquid Chromatography - Mass spectrometry (LC-MS) (Mackay et al., 2015). Briefly, extraction solution used was 50% methanol, 30% ACN, and 20% water. The volume

of extraction solution added was calculated from the weight of powdered tissue (30 mg: *in vivo* mouse and human livers) or from the number of cells for each condition (primary cultures). After addition of extraction solution, samples were vortexed for 5 minutes at 4 °C, and then centrifuged at 16,000 g for 15 minutes at 4 °C. The supernatants were collected and analyzed by LC-MS using SeQuant ZIC-pHilic column (Merck) for the liquid chromatography separation. Mobile phase A consisted of 20 mM ammonium carbonate plus 0.1% ammonia hydroxide in water. Mobile phase B consisted of ACN. The flow rate was kept at 100 mL/min, and the gradient was 0 min, 80% of B; 30 min, 20% of B; 31 min, 80% of B; and 45 min, 80% of B. The mass spectrometer (QExactive Plus Orbitrap, Thermo Fisher Scientific) was operated in a polarity-switching mode and metabolites were identified using TraceFinder Software (Thermo Fisher Scientific). For analyses, metabolomic data were normalized using the sum normalization method. MetaboAnalyst 4.0 software was used to conduct statistical analyses and heatmap generation, and unpaired two-sample t test was chosen to perform the comparisons (Chong and Xia, 2020). Quantities of each dNTP were used for histograms and statistical analyses.

Gene expression analysis and microarray

For mouse samples, total RNA from mouse primary hepatocyte cultures was extracted using Trizol Reagent (ThermoFischer Scientific #15596018). Sample concentration and purity were determined and then reverse-transcribed with the High-Capacity cDNA Reverse-Transcription Kit. Quantitative PCR (q-PCR) was performed using a SYBR Luminaris Color HiGreen qPCR master mix and specific primers (Supplementary Table 1) on 100 ng total RNA (ThermoFisher Scientific #4368813). The reactions were performed in 96-well plates in a LightCycler CFX connect (Biorad) during 40 cycles

with SYBR Luminaris Color HiGreen qPCR master mix (ThermoFisher Scientific #K0394). The relative amount of mRNAs was calculated using the Ct method, with LightCycler CFX analysis software, and normalized to the expression of 18S mRNA. For microarray analysis, all RNA processing steps, microarrays and statistical analysis were carried out by the Genom'IC facility (Institut Cochin, INSERM U1016, Paris, France). RNA quality was checked with a Bioanalyzer 2100 (with the Agilent RNA6000 pico chip kit). Reverse transcription was carried out on 400 pg of total RNA, following the Ovation Pico WTA System V2 (Nugen). Sens Target DNA (5 µg) were then hybridized to GeneChip® MTA1.0 (Affymetrix), washed and finally scanned using the GCS3000 7G. The scanned images were then analyzed with Expression Console software (Affymetrix) to obtain raw data (CEL Intensity files) and metrics for Quality Controls. A two-way analysis of variance (ANOVA) was applied to identify genes differentially expressed between the groups (SD *vs* HFHS or SD *vs* CDHFD) and fold changes were used to filter and select differentially expressed genes (>1.2). Global analysis was carried out by Gene Set Enrichment Analysis (GSEA). GSEA was performed using the fgsea package in R in order to identify gene sets overrepresented among up- and down-regulated genes. Human and murine gene sets were obtained from the Molecular Signatures Database (MSigDB) using the msigdbr package (version 6.2.1) Using a statistical analysis, the nominal p value and false discovery rate (q value) were defined, based on 1,000 random permutations between the different GeneSets studied. According to the software developers, results were significant for p value < 0.05 and q value < 0.25 (false discovery rate below 25%). Data are accessible on GEO #GSE154194.

For HepaRG: For gene expression analysis, $1.2x10^5$ cells were seeded per well of a 12-well plate in 1 ml assay medium. After attachment, for 24h, cells were treated as

indicative above. Then, cells were washed with PBS, and 300 µl of RLT Buffer (from RNeasy Kit, Qiagen #74104) was added. Samples were either stored at -80°C or RNA was extracted according to manufacturer's instructions. RNA concentration and quality were determined by Nanodrop analyzer. Isolated RNA was either stored at -80°C or was reverse transcribed for cDNA synthesis. For RNA sequencing, 25 ng RNA was sequenced by Dr.Rupert Öllinger, from AG Prof. Roland Rad.

For Human cohort, total liver RNA was extracted using the RNeasy Mini Kit (74104, Qiagen, Hilden, Germany) and treated with Turbo DNA-free (AM 1907, Thermo Fisher scientific Inc.) following the manufacturer's protocol. The quantity and quality of the RNAs were determined using the Agilent 2100 Bioanalyzer with RNA 6000 Nano Kit (5067-1511, Agilent Technologies, Santa Clara, CA, USA). Total RNA (1 µg) was reverse transcribed with a High-Capacity DNA Reverse Transcription Kit. Real-time quantitative PCR was performed in duplicate for each sample using the StepOne Plus Real-Time PCR System (Thermo Fisher scientific Inc.). TaqMan gene expression assays were purchased from Thermo Fisher Scientific Inc. (RPLP0: Hs99999902_m1; MB21D1/Cgas: Hs00403553_m1; TMEM173/STING-Hs00736955_g1). Gene expression was normalized to the housekeeping gene RPLP0 (Ribosomal Phosphoprotein Large P0, mouse and human) and calculated based on the comparative cycle threshold Ct method. Statistical significance of differential gene expression between two study groups was determined using the nonparametric Mann-Whitney test. Correlations were analyzed using the Pearson's correlation test. $p < 0.05$ was considered as significant.

***In vivo* histochemistry**

Mouse livers were fixed overnight in 10% neutral buffered formalin and then transferred in 70% ethanol for 24 hours, embedded in paraffin blocks, and finally cut in 3-µm-thick sections. After drying overnight at 37°C, liver sections were subsequently stained with Haematoxylin-Eosin-Saffron (HES) by an automated slide stainer (Thermo Fisher Scientific VARISTAIN Gemini ES). Histological grading was determined based on accepted human histopathological criteria for NAFLD. For PCNA/γH2AX staining: Liver sections (5µm) were deparaffinized and incubated in citrate buffer at 95°C for 20min for antigen retrieval. Sections were incubated overnight at 4°C with the primary antibodies including anti-γH2AX (1:200 dilution) and anti-PCNA (1:200 dilution) (See Supplementary Table 2). Anti-mouse or anti-rabbit IgG antibodies (1:500) conjugated with Alexa Fluor 488 or Alexa Fluor 594 (Thermo Fisher) were used as secondary antibodies. Hoechst 33342 (0.2 µg/mL; Merck #H3570) was included in the final wash to counterstain nuclei. All images were collected with the slide imager Zeiss Axio Scan Z1. At least 80 PCNA+ hepatocytes were analyzed regarding their γH2AX positivity in at least 3 different lobes per animal.

RNA *in situ* hybridization (RNAscope)

RNA *in situ* hybridization was done on freshly cut 5µm FFPE liver using the RNAScope 2.5 HD Duplex Kit (#322371), with HybEZ II hybridization system, following the manufacturer's instructions (Advanced Cell Diagnostics, Bio-Techne). The following RNAscope probe was used: RNAscope® Probe - Mm-Tmem173 - Mus musculus transmembrane protein 173 (Tmem173) mRNA (#413321). For the quantification, the number of dot (0, 1, 2, >3) have been counted in 500 hepatocytes per animal, localized in at least 10 different areas along the centro-lobular axis.

Immunoblot analysis

Hepatocytes cytoplasmic extracts were prepared using the NE-PER Nuclear and Cytoplasmic Extraction Reagent Kit (Thermo Fisher Scientific # 78833). Total proteins were extracted from mouse primary hepatocyte cultures in RIPA buffer (Merck #R0278) containing protease and phosphatase inhibitors (ThermoFischer Scientific #A32965 and Merck #35675). Protein concentration was determined using the bicinchoninic acid assay (BCA) (ThermoFisher Scientific #23225). Proteins (25 µg) were denatured in Laemmli buffer containing 5% β-mercaptoethanol, then separated by SDS-PAGE and blotted by semi-dry blotting (Trans-Blot Turbo Transfer, Bio Rad) onto nitrocellulose membranes (Bio Rad). To ensure equal loading, membranes were stained with Ponceau Red. Membranes were blocked in 5% milk/PBS-Tween (0.1%) for at least 1 hour at room temperature and then incubated at 4°C overnight under shaking conditions with primary antibodies (Supplemental Table 2). Incubation with the secondary antibody (HRP-anti-rabbit or HRP-anti-mouse, 1:2500) was performed under shaking conditions for 1 hour. Detection was achieved with Clarity Western ECL Substrate (Bio Rad) using the iBright CL1500 Imaging system (Thermo Fisher Scientific). In all immunoblotting, HSC70 or total protein were used to normalize the results. For protein quantification, densitometry analysis was performed using Image J. Data are presented as relative units, which represent the densitometric value for the protein of interest normalized to the second protein of interest.

***In vitro* Immunofluorescence**

Primary hepatocytes were fixed in 4% paraformaldehyde during 15 minutes for γH2AX/pHH3 and 53BP1 stainings or in cold fixative solution (75% ethanol 25% acetic acid) during 20 minutes for the BrdU labeling. The BrdU immunofluorescence was

images). Original magnification, ×20. The white bar indicates 20 µm. **(E)** Representation of the percentage of cells in G2/M phase (positive for pHH3) (*n*= 3 SD, 4 HFHS and 4 CDHFD). The data shown are the mean ± SEM. One-way ANOVA with Tukey's test for multiple comparisons. **(F)** Histogram representing the percentage of replicating hepatocytes (PCNA+) in liver parenchyma. One-way ANOVA (*n*=3 animals per group). One-way ANOVA test. **(G)** Histogram representing the percentage of damaged hepatocytes (γH2AX+). One-way ANOVA (*n*=3 animals per group).

Supplemental Figure 3 (related to Figures 2 and 3). Lipid overload in human hepatocytes leads to replication stress and DNA damage. (A) To induce steatosis, differentiated confluent HepaRG cells were treated for 4 days with a mixture of palmitic (33 µM) and oleic acid (66 µM) (FA-treated). Then, cells were trypsinized and plated again to induce proliferation. **(B)** Oil Red O staining (red) representing FA uptake by HepaRG. Representative images of 3 independent experiments. The black bar indicates 20 µm. **(C)** RNA sequencing analysis after 24h of treatment. The top upregulated pathways enriched in FA are shown. **(D)** Replication fork speed in untreated (UT) and FA condition. 60 fibers were analyzed for each experiment (*n*=3 experiments per group). Data represent the mean ± SEM. Each mean is indicated on the graph. Unpaired two-tailed *t*-test. **(E)** Quantification of the comet tails. Three representative experiments are presented with at least 50 nuclei counted per experiment. Results are presented as mean ± SEM. Unpaired two-tailed *t*-test. **(F)** Immunoblot analysis comparing the phosphorylation of H2AX in untreated and FA HepaRG cells. HSC70 was used as a loading control. The immunoblot is representative 4 independent experiments. **(G)** Quantification of γH2AX expression in UT and FA condition normalized on HSC70. Data represent the mean ± SEM. Mann-

Whitney test. **(H)** Relative levels of dNTPs (dATP, dCTP and dTTP) measured by LC-MS. The results are presented as the mean ± SEM. For each dNTP, unpaired two-tailed *t*-test. **(I)** Enrichment analysis representing *p*-values for the purine and pyrimidine pathways (FA vs UT). Metabolite set enrichment analysis was determined by LC-MS (*n*=4 per group).

Supplemental Figure 4 (related to Figure 4). Nucleotide metabolism reprogramming during the proliferation of steatotic hepatocytes. (A) GSEA showing the downregulated pathways, which are involved in nucleotide regulation and synthesis, in proliferating HFHS and CDHFD hepatocytes, at 48 hours of culture (normalized against SD with an enrichment score [ES] <-1.3 (red bars), *n*=3 animals per group). The *p*-value was determined with the GSEA program. **(B, C)** Enrichment-map representing fold enrichment and p-value of deregulated pathways in proliferating HFHS **(B)** and CDHFD **(C)** (at 48h of culture). Metabolite set enrichment analysis; from LC-MS experiment was obtained with the Metaboanalyst software. (*n*=6 SD, 4 HFHS; 4 CDHFD). **(D)** Relative levels of Nucleoside MonoPhosphate (NMPs: AMP, UMP, GMP and CMP) measured by LC-MS, at 48h of culture. The results are presented as the mean ± SEM. For each NMP, one-way ANOVA test with Tukey's Multiple Comparisons. **(E)** Relative levels of Nucleoside DiPhosphate (NDPs: ADP, UDP, GDP and CDP) measured by LC-MS, at 48h of culture. The results are presented as the mean ± SEM. For each NDP, one-way ANOVA test with Tukey's Multiple Comparisons, at 48h of culture. **(F)** Relative levels of dNTPs (dATP, dTTP and dCTP, respectively) measured by LC-MS, at 36h of culture. The results are presented as the mean ± SEM. For each dNTP, one-way ANOVA was performed with Tukey's test for multiple comparisons. **(G)** Quantification of the comet tail. Three dNTP recue

experiments are presented for HFHS and CDHFD primary hepatocytes, with 105 nuclei counted per experiment. Results are presented as the mean ± SEM and a Mann-Whitney *U* test was performed.

Supplemental Figure 5 (related to Figure 5). Replication stress promotes cGAS/STING pathway activation in NAFLD hepatocytes. (A) Percentage of cells displaying micronuclei at 60h of culture in *n*=3 independent experiments. Micronuclei have been quantified with the « operetta » microscope from Perkin Elmer based on Hoechst staining. **(B)** Immunoblot analysis of Histone H3 after cytoplasmic extraction. HSP70 is used as a loading control. **(C)** RT-qPCR to analyze *Sting (Tmem173)* expression during a time-course experiment (*n*=8 per groups), normalized against SD at 24 h. One-way ANOVA with Tukey tests. Asterisks indicate significant differences between time points. Dollar signs indicate significant differences at 60 h of culture. **(D)** RT-qPCR analysis of *Ifnβ*, *Isg15* and *Mx1* gene expression at 60 hours of culture. The data shown are the mean ± SEM (*n*=8 per group) normalized against SD. One-way ANOVA with Tukey tests.

References

Aguilera, A., García-Muse, T., 2013. Causes of genome instability. Annu. Rev. Genet. 47, 1–32. https://doi.org/10.1146/annurev-genet-111212-133232

Ahn, J., Xia, T., Konno, H., Konno, K., Ruiz, P., Barber, G.N., 2014. Inflammation-driven carcinogenesis is mediated through STING. Nat. Commun. 5, 5166. https://doi.org/10.1038/ncomms6166

Anstee, Q.M., Reeves, H.L., Kotsiliti, E., Govaere, O., Heikenwalder, M., 2019. From NASH to HCC: current concepts and future challenges. Nat. Rev. Gastroenterol. Hepatol. 16, 411–428. https://doi.org/10.1038/s41575-019-0145-7

Anstee, Q.M., Targher, G., Day, C.P., 2013. Progression of NAFLD to diabetes mellitus, cardiovascular disease or cirrhosis. Nat Rev Gastroenterol Hepatol 10, 330–44. https://doi.org/10.1038/nrgastro.2013.41

Aravinthan, A., Scarpini, C., Tachtatzis, P., Verma, S., Penrhyn-Lowe, S., Harvey, R., Davies, S.E., Allison, M., Coleman, N., Alexander, G., 2013. Hepatocyte senescence predicts progression in non-alcohol-related fatty liver disease. J. Hepatol. 58, 549–556. https://doi.org/10.1016/j.jhep.2012.10.031

Baffy, G., Brunt, E.M., Caldwell, S.H., 2012. Hepatocellular carcinoma in non-alcoholic fatty liver disease: an emerging menace. J Hepatol 56, 1384–91.

Bedossa, P., Poitou, C., Veyrie, N., Bouillot, J.-L., Basdevant, A., Paradis, V., Tordjman, J., Clement, K., 2012. Histopathological algorithm and scoring system for evaluation of liver lesions in morbidly obese patients. Hepatol. Baltim. Md 56, 1751–1759. https://doi.org/10.1002/hep.25889

Begriche, K., Massart, J., Robin, M.-A., Bonnet, F., Fromenty, B., 2013. Mitochondrial adaptations and dysfunctions in nonalcoholic fatty liver disease. Hepatol. Baltim. Md 58, 1497–1507. https://doi.org/10.1002/hep.26226

Bester, A.C., Roniger, M., Oren, Y.S., Im, M.M., Sarni, D., Chaoat, M., Bensimon, A., Zamir, G., Shewach, D.S., Kerem, B., 2011. Nucleotide deficiency promotes genomic instability in early stages of cancer development. Cell 145, 435–446. https://doi.org/10.1016/j.cell.2011.03.044

Boege, Y., Malehmir, M., Healy, M.E., Bettermann, K., Lorentzen, A., Vucur, M., Ahuja, A.K., Böhm, F., Mertens, J.C., Shimizu, Y., Frick, L., Remouchamps, C., Mutreja, K., Kähne, T., Sundaravinayagam, D., Wolf, M.J., Rehrauer, H., Koppe, C., Speicher, T., Padrissa-Altés, S., Maire, R., Schattenberg, J.M., Jeong, J.-S., Liu, L., Zwirner, S., Boger, R., Hüser, N., Davis, R.J., Müllhaupt, B., Moch, H., Schulze-Bergkamen, H., Clavien, P.-A., Werner, S., Borsig, L., Luther, S.A., Jost, P.J., Weinlich, R., Unger, K., Behrens, A., Hillert, L., Dillon, C., Di Virgilio, M., Wallach, D., Dejardin, E., Zender, L., Naumann, M., Walczak, H., Green, D.R., Lopes, M., Lavrik, I., Luedde, T., Heikenwalder, M., Weber, A., 2017. A Dual Role of Caspase-8 in Triggering and Sensing Proliferation-Associated DNA Damage, a Key Determinant of Liver Cancer Development. Cancer Cell 32, 342-359.e10. https://doi.org/10.1016/j.ccell.2017.08.010

Brunt, E.M., Janney, C.G., Di Bisceglie, A.M., Neuschwander-Tetri, B.A., Bacon, B.R., 1999. Nonalcoholic steatohepatitis: a proposal for grading and staging the histological lesions. Am J Gastroenterol 94, 2467–74. https://doi.org/10.1111/j.1572-0241.1999.01377.x

Brunt, E.M., Kleiner, D.E., 2017. Challenges in the hepatic histopathology in non-alcoholic fatty liver disease. Gut 66, 1539–1540. https://doi.org/10.1136/gutjnl-2016-313379

Buzzetti, E., Pinzani, M., Tsochatzis, E.A., 2016. The multiple-hit pathogenesis of non-alcoholic fatty liver disease (NAFLD). Metabolism. https://doi.org/10.1016/j.metabol.2015.12.012

Chabosseau, P., Buhagiar-Labarchède, G., Onclercq-Delic, R., Lambert, S., Debatisse, M., Brison, O., Amor-Guéret, M., 2011. Pyrimidine pool imbalance induced by BLM helicase deficiency contributes to genetic instability in Bloom syndrome. Nat. Commun. 2, 368. https://doi.org/10.1038/ncomms1363

Chong, J., Xia, J., 2020. Using MetaboAnalyst 4.0 for Metabolomics Data Analysis, Interpretation, and Integration with Other Omics Data. Methods Mol. Biol. Clifton NJ 2104, 337–360. https://doi.org/10.1007/978-1-0716-0239-3_17

Collin de l'Hortet, A., Zerrad-Saadi, A., Prip-Buus, C., Fauveau, V., Helmy, N., Ziol, M., Vons, C., Billot, K., Baud, V., Gilgenkrantz, H., Guidotti, J.-E., 2014. GH administration rescues fatty liver regeneration impairment by restoring GH/EGFR pathway deficiency. Endocrinology 155, 2545–2554. https://doi.org/10.1210/en.2014-1010

Coquel, F., Silva, M.-J., Técher, H., Zadorozhny, K., Sharma, S., Nieminuszczy, J., Mettling, C., Dardillac, E., Barthe, A., Schmitz, A.-L., Promonet, A., Cribier, A., Sarrazin, A., Niedzwiedz, W., Lopez, B., Costanzo, V., Krejci, L., Chabes, A., Benkirane, M., Lin, Y.-L., Pasero, P., 2018. SAMHD1 acts at stalled replication forks to prevent interferon induction. Nature 557, 57–61. https://doi.org/10.1038/s41586-018-0050-1

Diehl, A.M., Day, C., 2017. Cause, Pathogenesis, and Treatment of Nonalcoholic Steatohepatitis. N. Engl. J. Med. 377, 2063–2072. https://doi.org/10.1056/NEJMra1503519

Diehl, F.F., Lewis, C.A., Fiske, B.P., Vander Heiden, M.G., 2019. Cellular redox state constrains serine synthesis and nucleotide production to impact cell proliferation. Nat. Metab. 1, 861–867. https://doi.org/10.1038/s42255-019-0108-x

Donati, B., Pietrelli, A., Pingitore, P., Dongiovanni, P., Caddeo, A., Walker, L., Baselli, G., Pelusi, S., Rosso, C., Vanni, E., Daly, A., Mancina, R.M., Grieco, A., Miele, L., Grimaudo, S., Craxi, A., Petta, S., De Luca, L., Maier, S., Soardo, G., Bugianesi, E., Colli, F., Romagnoli, R., Anstee, Q.M., Reeves, H.L., Fracanzani, A.L., Fargion, S., Romeo, S., Valenti, L., 2017. Telomerase reverse transcriptase germline mutations and hepatocellular carcinoma in patients with nonalcoholic fatty liver disease. Cancer Med. 6, 1930–1940. https://doi.org/10.1002/cam4.1078

Donnelly, K.L., Smith, C.I., Schwarzenberg, S.J., Jessurun, J., Boldt, M.D., Parks, E.J., 2005. Sources of fatty acids stored in liver and secreted via lipoproteins in patients with nonalcoholic fatty liver disease. J. Clin. Invest. 115, 1343–1351. https://doi.org/10.1172/JCI23621

Duncan, A.W., Taylor, M.H., Hickey, R.D., Hanlon Newell, A.E., Lenzi, M.L., Olson, S.B., Finegold, M.J., Grompe, M., 2010. The ploidy conveyor of mature hepatocytes as a source of genetic variation. Nature 467, 707–710. https://doi.org/10.1038/nature09414

Eslam, M., Sanyal, A.J., George, J., International Consensus Panel, 2020. MAFLD: A Consensus-Driven Proposed Nomenclature for Metabolic Associated Fatty Liver Disease. Gastroenterology 158, 1999-2014.e1. https://doi.org/10.1053/j.gastro.2019.11.312

Estes, C., Razavi, H., Loomba, R., Younossi, Z., Sanyal, A.J., 2018. Modeling the epidemic of nonalcoholic fatty liver disease demonstrates an exponential increase in burden of disease. Hepatol. Baltim. Md 67, 123–133. https://doi.org/10.1002/hep.29466

Fingas, C.D., Best, J., Sowa, J.P., Canbay, A., 2016. Epidemiology of nonalcoholic steatohepatitis and hepatocellular carcinoma. Clin Liver Hoboken 8, 119–122. https://doi.org/10.1002/cld.585

Fortier, M., Celton-Morizur, S., Desdouets, C., 2017. Incomplete cytokinesis/binucleation in mammals: The powerful system of hepatocytes. Methods Cell Biol 137, 119–142. https://doi.org/10.1016/bs.mcb.2016.04.006

Friedman, S.L., Neuschwander-Tetri, B.A., Rinella, M., Sanyal, A.J., 2018. Mechanisms of NAFLD development and therapeutic strategies. Nat. Med. 24, 908–922. https://doi.org/10.1038/s41591-018-0104-9

Gaillard, H., García-Muse, T., Aguilera, A., 2015. Replication stress and cancer. Nat. Rev. Cancer 15, 276–289. https://doi.org/10.1038/nrc3916

Gentric, G., Desdouets, C., 2015. Liver polyploidy: Dr Jekyll or Mr Hide? Oncotarget 6, 8430–8431. https://doi.org/10.18632/oncotarget.3809

Gentric, G., Maillet, V., Paradis, V., Couton, D., L'Hermitte, A., Panasyuk, G., Fromenty, B., Celton-Morizur, S., Desdouets, C., 2015. Oxidative stress promotes pathologic polyploidization in nonalcoholic fatty liver disease. J. Clin. Invest. 125, 981–992. https://doi.org/10.1172/JCI73957

Gomes, A.L., Teijeiro, A., Burén, S., Tummala, K.S., Yilmaz, M., Waisman, A., Theurillat, J.-P., Perna, C., Djouder, N., 2016. Metabolic Inflammation-Associated IL-17A Causes Non-alcoholic Steatohepatitis and Hepatocellular Carcinoma. Cancer Cell 30, 161–175. https://doi.org/10.1016/j.ccell.2016.05.020

Gripon, P., Rumin, S., Urban, S., Le Seyec, J., Glaise, D., Cannie, I., Guyomard, C., Lucas, J., Trepo, C., Guguen-Guillouzo, C., 2002. Infection of a human hepatoma cell line by hepatitis B virus. Proc. Natl. Acad. Sci. U. S. A. 99, 15655–15660. https://doi.org/10.1073/pnas.232137699

Gyori, B.M., Venkatachalam, G., Thiagarajan, P.S., Hsu, D., Clement, M.-V., 2014. OpenComet: an automated tool for comet assay image analysis. Redox Biol. 2, 457–465. https://doi.org/10.1016/j.redox.2013.12.020

Hsu, S.H., Delgado, E.R., Otero, P.A., Teng, K.Y., Kutay, H., Meehan, K.M., Moroney, J.B., Monga, J.K., Hand, N.J., Friedman, J.R., Ghoshal, K., Duncan, A.W., 2016. MicroRNA-122 Regulates Polyploidization in the Murine Liver. Hepatology. https://doi.org/10.1002/hep.28573

Kim, J.Y., Garcia-Carbonell, R., Yamachika, S., Zhao, P., Dhar, D., Loomba, R., Kaufman, R.J., Saltiel, A.R., Karin, M., 2018. ER Stress Drives Lipogenesis and Steatohepatitis via Caspase-2 Activation of S1P. Cell 175, 133-145.e15. https://doi.org/10.1016/j.cell.2018.08.020

Kleiner, D.E., Brunt, E.M., Van Natta, M., Behling, C., Contos, M.J., Cummings, O.W., Ferrell, L.D., Liu, Y.-C., Torbenson, M.S., Unalp-Arida, A., Yeh, M., McCullough, A.J., Sanyal, A.J., Nonalcoholic Steatohepatitis Clinical Research Network, 2005. Design and validation of a histological scoring system for nonalcoholic fatty liver disease. Hepatol. Baltim. Md 41, 1313–1321. https://doi.org/10.1002/hep.20701

Kwon, J., Bakhoum, S.F., 2020. The Cytosolic DNA-Sensing cGAS-STING Pathway in Cancer. Cancer Discov. 10, 26–39. https://doi.org/10.1158/2159-8290.CD-19-0761

Lebeaupin, C., Vallée, D., Hazari, Y., Hetz, C., Chevet, E., Bailly-Maitre, B., 2018. Endoplasmic reticulum stress signalling and the pathogenesis of non-alcoholic fatty liver disease. J. Hepatol. 69, 927–947. https://doi.org/10.1016/j.jhep.2018.06.008

Lebofsky, R., Bensimon, A., 2005. DNA replication origin plasticity and perturbed fork progression in human inverted repeats. Mol Cell Biol 25, 6789–97. https://doi.org/10.1128/MCB.25.15.6789-6797.2005

Leclercq, I.A., Vansteenberghe, M., Lebrun, V.B., VanHul, N.K., Abarca-Quinones, J., Sempoux, C.L., Picard, C., Starkel, P., Horsmans, Y.L., 2006. Defective hepatic regeneration after partial hepatectomy in leptin-deficient mice is not rescued by exogenous leptin. Lab Invest 86, 1161–71.

Li, T., Chen, Z.J., 2018. The cGAS-cGAMP-STING pathway connects DNA damage to inflammation, senescence, and cancer. J Exp Med 215, 1287–1299. https://doi.org/10.1084/jem.20180139

López-Contreras, A.J., Fernandez-Capetillo, O., 2010. The ATR barrier to replication-born DNA damage. DNA Repair 9, 1249–1255. https://doi.org/10.1016/j.dnarep.2010.09.012

Lukas, C., Savic, V., Bekker-Jensen, S., Doil, C., Neumann, B., Pedersen, R.S., Grofte, M., Chan, K.L., Hickson, I.D., Bartek, J., Lukas, J., 2011. 53BP1 nuclear bodies form around DNA lesions generated by mitotic transmission of chromosomes under replication stress. Nat Cell Biol 13, 243–53. https://doi.org/10.1038/ncb2201

Luo, X., Li, H., Ma, L., Zhou, J., Guo, X., Woo, S.-L., Pei, Y., Knight, L.R., Deveau, M., Chen, Y., Qian, X., Xiao, X., Li, Q., Chen, X., Huo, Y., McDaniel, K., Francis, H., Glaser, S., Meng, F., Alpini, G., Wu, C., 2018. Expression of STING Is Increased in Liver Tissues From Patients With NAFLD and Promotes Macrophage-Mediated Hepatic Inflammation and Fibrosis in Mice. Gastroenterology 155, 1971-1984.e4. https://doi.org/10.1053/j.gastro.2018.09.010

Mackay, G.M., Zheng, L., van den Broek, N.J.F., Gottlieb, E., 2015. Analysis of Cell Metabolism Using LC-MS and Isotope Tracers. Methods Enzymol. 561, 171–196. https://doi.org/10.1016/bs.mie.2015.05.016

Magdalou, I., Lopez, B.S., Pasero, P., Lambert, S.A.E., 2014. The causes of replication stress and their consequences on genome stability and cell fate. Semin. Cell Dev. Biol., Regulation of Spermatogenesis Part II & DNA Replication 30, 154–164. https://doi.org/10.1016/j.semcdb.2014.04.035

Malehmir, M., Pfister, D., Gallage, S., Szydlowska, M., Inverso, D., Kotsiliti, E., Leone, V., Peiseler, M., Surewaard, B.G.J., Rath, D., Ali, A., Wolf, M.J., Drescher, H., Healy, M.E., Dauch, D., Kroy, D., Krenkel, O., Kohlhepp, M., Engleitner, T., Olkus, A., Sijmonsma, T., Volz, J., Deppermann, C., Stegner, D., Helbling, P., Nombela-Arrieta, C., Rafiei, A., Hinterleitner, M., Rall, M., Baku, F., Borst, O., Wilson, C.L., Leslie, J., O'Connor, T., Weston, C.J., Adams, D.H., Sheriff, L., Teijeiro, A., Prinz, M., Bogeska, R., Anstee, N., Bongers, M.N., Notohamiprodjo, M., Geisler, T., Withers, D.J., Ware, J., Mann, D.A., Augustin, H.G., Vegiopoulos, A., Milsom, M.D., Rose, A.J., Lalor, P.F., Llovet, J.M., Pinyol, R., Tacke, F., Rad, R., Matter, M., Djouder, N., Kubes, P., Knolle, P.A., Unger, K., Zender, L., Nieswandt, B., Gawaz, M., Weber, A., Heikenwalder, M., 2019. Platelet GPIbα is a mediator and potential interventional target for NASH and subsequent liver cancer. Nat. Med. 25, 641–655. https://doi.org/10.1038/s41591-019-0379-5

Margall-Ducos, G., Celton-Morizur, S., Couton, D., Brégerie, O., Desdouets, C., 2007. Liver tetraploidization is controlled by a new process of incomplete cytokinesis. J. Cell Sci. 120, 3633–3639. https://doi.org/10.1242/jcs.016907

Michalet, X., Ekong, R., Fougerousse, F., Rousseaux, S., Schurra, C., Hornigold, N., van Slegtenhorst, M., Wolfe, J., Povey, S., Beckmann, J.S., Bensimon, A., 1997. Dynamic molecular combing: stretching the whole human genome for high-resolution studies. Science 277, 1518–1523.

Mokrani-Benhelli, H., Gaillard, L., Biasutto, P., Le Guen, T., Touzot, F., Vasquez, N., Komatsu, J., Conseiller, E., Picard, C., Gluckman, E., Francannet, C., Fischer, A., Durandy, A., Soulier,

J., de Villartay, J.P., Cavazzana-Calvo, M., Revy, P., 2013. Primary microcephaly, impaired DNA replication, and genomic instability caused by compound heterozygous ATR mutations. Hum Mutat 34, 374–84. https://doi.org/10.1002/humu.22245

Mota, M., Banini, B.A., Cazanave, S.C., Sanyal, A.J., 2016. Molecular mechanisms of lipotoxicity and glucotoxicity in nonalcoholic fatty liver disease. Metabolism 65, 1049–61. https://doi.org/10.1016/j.metabol.2016.02.014

Nakagawa, H., Umemura, A., Taniguchi, K., Font-Burgada, J., Dhar, D., Ogata, H., Zhong, Z., Valasek, M.A., Seki, E., Hidalgo, J., Koike, K., Kaufman, R.J., Karin, M., 2014. ER stress cooperates with hypernutrition to trigger TNF-dependent spontaneous HCC development. Cancer Cell 26, 331–343. https://doi.org/10.1016/j.ccr.2014.07.001

Nakajima, T., Nakashima, T., Okada, Y., Jo, M., Nishikawa, T., Mitsumoto, Y., Katagishi, T., Kimura, H., Itoh, Y., Kagawa, K., Yoshikawa, T., 2010. Nuclear size measurement is a simple method for the assessment of hepatocellular aging in non-alcoholic fatty liver disease: Comparison with telomere-specific quantitative FISH and p21 immunohistochemistry. Pathol Int 60, 175–83. https://doi.org/10.1111/j.1440-1827.2009.02504.x

Nishida, N., Yada, N., Hagiwara, S., Sakurai, T., Kitano, M., Kudo, M., 2016. Unique features associated with hepatic oxidative DNA damage and DNA methylation in non-alcoholic fatty liver disease. J. Gastroenterol. Hepatol. 31, 1646–1653. https://doi.org/10.1111/jgh.13318

Norbury, C., Blow, J., Nurse, P., 1991. Regulatory phosphorylation of the p34cdc2 protein kinase in vertebrates. Embo J 10, 3321–9.

Ogrodnik, M., Miwa, S., Tchkonia, T., Tiniakos, D., Wilson, C.L., Lahat, A., Day, C.P., Burt, A., Palmer, A., Anstee, Q.M., Grellscheid, S.N., Hoeijmakers, J.H.J., Barnhoorn, S., Mann, D.A., Bird, T.G., Vermeij, W.P., Kirkland, J.L., Passos, J.F., von Zglinicki, T., Jurk, D., 2017. Cellular senescence drives age-dependent hepatic steatosis. Nat. Commun. 8, 15691. https://doi.org/10.1038/ncomms15691

Orvain, C., Lin, Y.-L., Jean-Louis, F., Hocini, H., Hersant, B., Bennasser, Y., Ortonne, N., Hotz, C., Wolkenstein, P., Boniotto, M., Tisserand, P., Lefebvre, C., Lelièvre, J.-D., Benkirane, M., Pasero, P., Lévy, Y., Hüe, S., 2020. Hair follicle stem cell replication stress drives IFI16/STING-dependent inflammation in hidradenitis suppurativa. J. Clin. Invest. 130, 3777–3790. https://doi.org/10.1172/JCI131180

Parkes, E.E., Walker, S.M., Taggart, L.E., McCabe, N., Knight, L.A., Wilkinson, R., McCloskey, K.D., Buckley, N.E., Savage, K.I., Salto-Tellez, M., McQuaid, S., Harte, M.T., Mullan, P.B., Harkin, D.P., Kennedy, R.D., 2017. Activation of STING-Dependent Innate Immune Signaling By S-Phase-Specific DNA Damage in Breast Cancer. J. Natl. Cancer Inst. 109. https://doi.org/10.1093/jnci/djw199

Patouraux, S., Rousseau, D., Bonnafous, S., Lebeaupin, C., Luci, C., Canivet, C.M., Schneck, A.-S., Bertola, A., Saint-Paul, M.-C., Iannelli, A., Gugenheim, J., Anty, R., Tran, A., Bailly-Maitre, B., Gual, P., 2017. CD44 is a key player in non-alcoholic steatohepatitis. J. Hepatol. 67, 328–338. https://doi.org/10.1016/j.jhep.2017.03.003

Pinyol, R., Torrecilla, S., Wang, H., Montironi, C., Piqué-Gili, M., Torres-Martin, M., Wei-Qiang, L., Willoughby, C.E., Ramadori, P., Andreu-Oller, C., Taik, P., Lee, Y.A., Moeini, A., Peix, J., Faure-Dupuy, S., Riedl, T., Schuehle, S., Oliveira, C.P., Alves, V.A., Boffetta, P., Lachenmayer, A., Roessler, S., Minguez, B., Schirmacher, P., Dufour, J.-F., Thung, S.N., Reeves, H.L., Carrilho, F.J., Chang, C., Uzilov, A.V., Heikenwalder, M., Sanyal, A., Friedman, S.L., Sia, D., Llovet, J.M., 2021. Molecular characterisation of hepatocellular

carcinoma in patients with non-alcoholic steatohepatitis. J. Hepatol. S0168-8278(21)00326–3. https://doi.org/10.1016/j.jhep.2021.04.049

Poli, J., Tsaponina, O., Crabbé, L., Keszthelyi, A., Pantesco, V., Chabes, A., Lengronne, A., Pasero, P., 2012. dNTP pools determine fork progression and origin usage under replication stress. EMBO J. 31, 883–894. https://doi.org/10.1038/emboj.2011.470

Ragu, S., Matos-Rodrigues, G., Lopez, B.S., 2020. Replication Stress, DNA Damage, Inflammatory Cytokines and Innate Immune Response. Genes 11. https://doi.org/10.3390/genes11040409

Rappez, L., Stadler, M., Triana, S., Gathungu, R.M., Ovchinnikova, K., Phapale, P., Heikenwalder, M., Alexandrov, T., 2021. SpaceM reveals metabolic states of single cells. Nat. Methods 18, 799–805. https://doi.org/10.1038/s41592-021-01198-0

Richardson, M.M., Jonsson, J.R., Powell, E.E., Brunt, E.M., Neuschwander-Tetri, B.A., Bhathal, P.S., Dixon, J.B., Weltman, M.D., Tilg, H., Moschen, A.R., Purdie, D.M., Demetris, A.J., Clouston, A.D., 2007. Progressive fibrosis in nonalcoholic steatohepatitis: association with altered regeneration and a ductular reaction. Gastroenterology 133, 80–90. https://doi.org/10.1053/j.gastro.2007.05.012

Rimmele, P., Komatsu, J., Hupe, P., Roulin, C., Barillot, E., Dutreix, M., Conseiller, E., Bensimon, A., Moreau-Gachelin, F., Guillouf, C., 2010. Spi-1/PU.1 oncogene accelerates DNA replication fork elongation and promotes genetic instability in the absence of DNA breakage. Cancer Res 70, 6757–66. https://doi.org/10.1158/0008-5472.CAN-09-4691

Saldivar, J.C., Cortez, D., Cimprich, K.A., 2017. The essential kinase ATR: ensuring faithful duplication of a challenging genome. Nat. Rev. Mol. Cell Biol. 18, 622–636. https://doi.org/10.1038/nrm.2017.67

Schild-Poulter, C., Su, A., Shih, A., Kelly, O.P., Fritzler, M.J., Goldstein, R., Haché, R.J.G., 2008. Association of autoantibodies with Ku and DNA repair proteins in connective tissue diseases. Rheumatol. Oxf. Engl. 47, 165–171. https://doi.org/10.1093/rheumatology/kem338

Schoggins, J.W., MacDuff, D.A., Imanaka, N., Gainey, M.D., Shrestha, B., Eitson, J.L., Mar, K.B., Richardson, R.B., Ratushny, A.V., Litvak, V., Dabelic, R., Manicassamy, B., Aitchison, J.D., Aderem, A., Elliott, R.M., Garcia-Sastre, A., Racaniello, V., Snijder, E.J., Yokoyama, W.M., Diamond, M.S., Virgin, H.W., Rice, C.M., 2014. Pan-viral specificity of IFN-induced genes reveals new roles for cGAS in innate immunity. Nature 505, 691–5. https://doi.org/10.1038/nature12862

Schults, M.A., Nagle, P.W., Rensen, S.S., Godschalk, R.W., Munnia, A., Peluso, M., Claessen, S.M., Greve, J.W., Driessen, A., Verdam, F.J., Buurman, W.A., van Schooten, F.J., Chiu, R.K., 2012. Decreased nucleotide excision repair in steatotic livers associates with myeloperoxidase-immunoreactivity. Mutat. Res. 736, 75–81. https://doi.org/10.1016/j.mrfmmm.2011.11.001

Schwabe, R.F., Luedde, T., 2018. Apoptosis and necroptosis in the liver: a matter of life and death. Nat. Rev. Gastroenterol. Hepatol. 15, 738–752. https://doi.org/10.1038/s41575-018-0065-y

Singh, S., Allen, A.M., Wang, Z., Prokop, L.J., Murad, M.H., Loomba, R., 2015. Fibrosis progression in nonalcoholic fatty liver vs nonalcoholic steatohepatitis: a systematic review and meta-analysis of paired-biopsy studies. Clin Gastroenterol Hepatol 13, 643-54 e1–9; quiz e39-40. https://doi.org/10.1016/j.cgh.2014.04.014

Taliento, E., Dallio, M., Frederico, A., Valenti, L., 2019. Novel Insights Into the Genetic Landscape of Nonalcoholic Fatty Liver Disease. Int J Env. Res Public Health 1, 1–13.

Tan, X., Sun, L., Chen, J., Chen, Z.J., 2018. Detection of Microbial Infections Through Innate Immune Sensing of Nucleic Acids. Annu Rev Microbiol 72, 447–478. https://doi.org/10.1146/annurev-micro-102215-095605

Tanaka, S., Miyanishi, K., Kobune, M., Kawano, Y., Hoki, T., Kubo, T., Hayashi, T., Sato, T., Sato, Y., Takimoto, R., Kato, J., 2013. Increased hepatic oxidative DNA damage in patients with nonalcoholic steatohepatitis who develop hepatocellular carcinoma. J. Gastroenterol. 48, 1249–1258. https://doi.org/10.1007/s00535-012-0739-0

Techer, H., Koundrioukoff, S., Nicolas, A., Debatisse, M., 2017. The impact of replication stress on replication dynamics and DNA damage in vertebrate cells. Nat Rev Genet 18, 535–550. https://doi.org/10.1038/nrg.2017.46

Tilg, H., Moschen, A.R., 2010. Evolution of inflammation in nonalcoholic fatty liver disease: the multiple parallel hits hypothesis. Hepatology 52, 1836–46. https://doi.org/10.1002/hep.24001

Toledo, L.I., Altmeyer, M., Rask, M.-B., Lukas, C., Larsen, D.H., Povlsen, L.K., Bekker-Jensen, S., Mailand, N., Bartek, J., Lukas, J., 2013. ATR prohibits replication catastrophe by preventing global exhaustion of RPA. Cell 155, 1088–1103. https://doi.org/10.1016/j.cell.2013.10.043

Valenti, L.V.C., Baselli, G.A., 2018. Genetics of Nonalcoholic Fatty Liver Disease: A 2018 Update. Curr Pharm Des 24, 4566–4573. https://doi.org/10.2174/1381612825666190119113836

Verbeek, J., Lannoo, M., Pirinen, E., Ryu, D., Spincemaille, P., Vander Elst, I., Windmolders, P., Thevissen, K., Cammue, B.P.A., van Pelt, J., Fransis, S., Van Eyken, P., Ceuterick-De Groote, C., Van Veldhoven, P.P., Bedossa, P., Nevens, F., Auwerx, J., Cassiman, D., 2015. Roux-en-y gastric bypass attenuates hepatic mitochondrial dysfunction in mice with non-alcoholic steatohepatitis. Gut 64, 673–683. https://doi.org/10.1136/gutjnl-2014-306748

Wang, X., Li, J., Riaz, D.R., Shi, G., Liu, C., Dai, Y., 2014. Outcomes of liver transplantation for nonalcoholic steatohepatitis: a systematic review and meta-analysis. Clin Gastroenterol Hepatol 12, 394-402 e1. https://doi.org/10.1016/j.cgh.2013.09.023

Wang, X., Rao, H., Zhao, J., Wee, A., Li, X., Fei, R., Huang, R., Wu, C., Liu, F., Wei, L., 2020. STING expression in monocyte-derived macrophages is associated with the progression of liver inflammation and fibrosis in patients with nonalcoholic fatty liver disease. Lab. Investig. J. Tech. Methods Pathol. 100, 542–552. https://doi.org/10.1038/s41374-019-0342-6

Wegermann, K., Diehl, A.M., Moylan, C.A., 2018. Disease pathways and molecular mechanisms of nonalcoholic steatohepatitis. Clin Liver Hoboken 11, 87–91. https://doi.org/10.1002/cld.709

Wirth, K.G., Wutz, G., Kudo, N.R., Desdouets, C., Zetterberg, A., Taghybeeglu, S., Seznec, J., Ducos, G.M., Ricci, R., Firnberg, N., Peters, J.M., Nasmyth, K., 2006. Separase: a universal trigger for sister chromatid disjunction but not chromosome cycle progression. J Cell Biol 172, 847–60.

Wolf, M.J., Adili, A., Piotrowitz, K., Abdullah, Z., Boege, Y., Stemmer, K., Ringelhan, M., Simonavicius, N., Egger, M., Wohlleber, D., Lorentzen, A., Einer, C., Schulz, S., Clavel, T., Protzer, U., Thiele, C., Zischka, H., Moch, H., Tschöp, M., Tumanov, A.V., Haller, D., Unger, K., Karin, M., Kopf, M., Knolle, P., Weber, A., Heikenwalder, M., 2014. Metabolic activation of intrahepatic CD8+ T cells and NKT cells causes nonalcoholic steatohepatitis and liver cancer via cross-talk with hepatocytes. Cancer Cell 26, 549–564. https://doi.org/10.1016/j.ccell.2014.09.003

Wong, R.J., Cheung, R., Ahmed, A., 2014. Nonalcoholic steatohepatitis is the most rapidly growing indication for liver transplantation in patients with hepatocellular carcinoma in the U.S. Hepatology 59, 2188–95. https://doi.org/10.1002/hep.26986

Yang, S., Koteish, A., Lin, H., Huang, J., Roskams, T., Dawson, V., Diehl, A.M., 2004. Oval cells compensate for damage and replicative senescence of mature hepatocytes in mice with fatty liver disease. Hepatology 39, 403–11.

Yang, Y.-G., Lindahl, T., Barnes, D.E., 2007. Trex1 exonuclease degrades ssDNA to prevent chronic checkpoint activation and autoimmune disease. Cell 131, 873–886. https://doi.org/10.1016/j.cell.2007.10.017

Younossi, Z., Anstee, Q.M., Marietti, M., Hardy, T., Henry, L., Eslam, M., George, J., Bugianesi, E., 2018. Global burden of NAFLD and NASH: trends, predictions, risk factors and prevention. Nat. Rev. Gastroenterol. Hepatol. 15, 11–20. https://doi.org/10.1038/nrgastro.2017.109

Younossi, Z.M., Koenig, A.B., Abdelatif, D., Fazel, Y., Henry, L., Wymer, M., 2016. Global epidemiology of nonalcoholic fatty liver disease-Meta-analytic assessment of prevalence, incidence, and outcomes. Hepatology 64, 73–84. https://doi.org/10.1002/hep.28431

Yu, Q., Katlinskaya, Y.V., Carbone, C.J., Zhao, B., Katlinski, K.V., Zheng, H., Guha, M., Li, N., Chen, Q., Yang, T., Lengner, C.J., Greenberg, R.A., Johnson, F.B., Fuchs, S.Y., 2015. DNA-damage-induced type I interferon promotes senescence and inhibits stem cell function. Cell Rep. 11, 785–797. https://doi.org/10.1016/j.celrep.2015.03.069

Yu, Y., Liu, Y., An, W., Song, J., Zhang, Y., Zhao, X., 2019. STING-mediated inflammation in Kupffer cells contributes to progression of nonalcoholic steatohepatitis. J. Clin. Invest. 129, 546–555. https://doi.org/10.1172/JCI121842

Zeman, M.K., Cimprich, K.A., 2014. Causes and consequences of replication stress. Nat. Cell Biol. 16, 2–9. https://doi.org/10.1038/ncb2897

Zhu, J., Thompson, C.B., 2019. Metabolic regulation of cell growth and proliferation. Nat. Rev. Mol. Cell Biol. 20, 436–450. https://doi.org/10.1038/s41580-019-0123-5

A

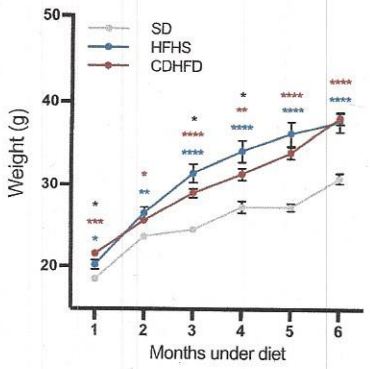
SD
HFHS
CDHFD
Weight (g)
Months under diet

B

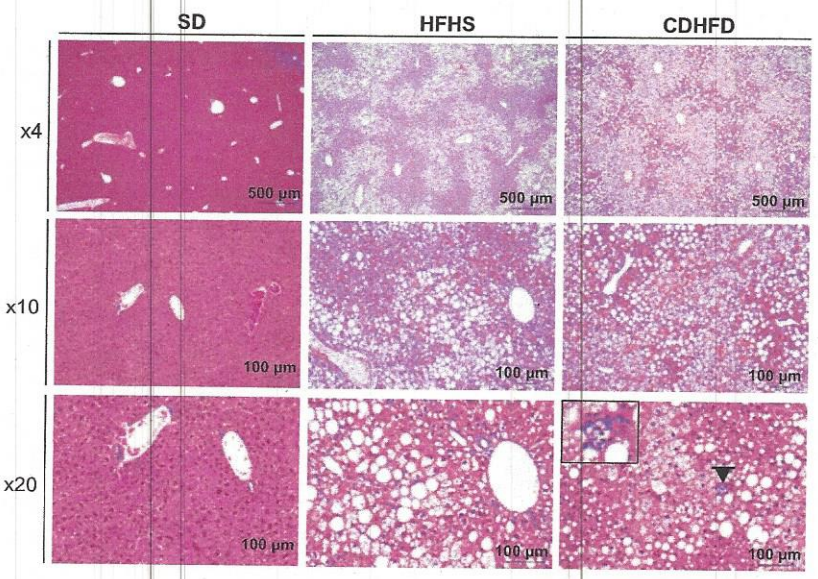
SD
HFHS
CDHFD
x4
x10
x20
500 µm
100 µm

C

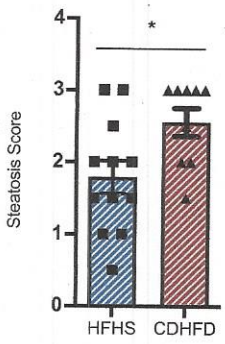
Steatosis Score
HFHS
CDHFD

D

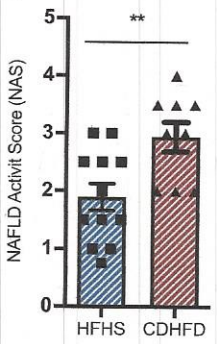
NAFLD Activit Score (NAS)
HFHS
CDHFD

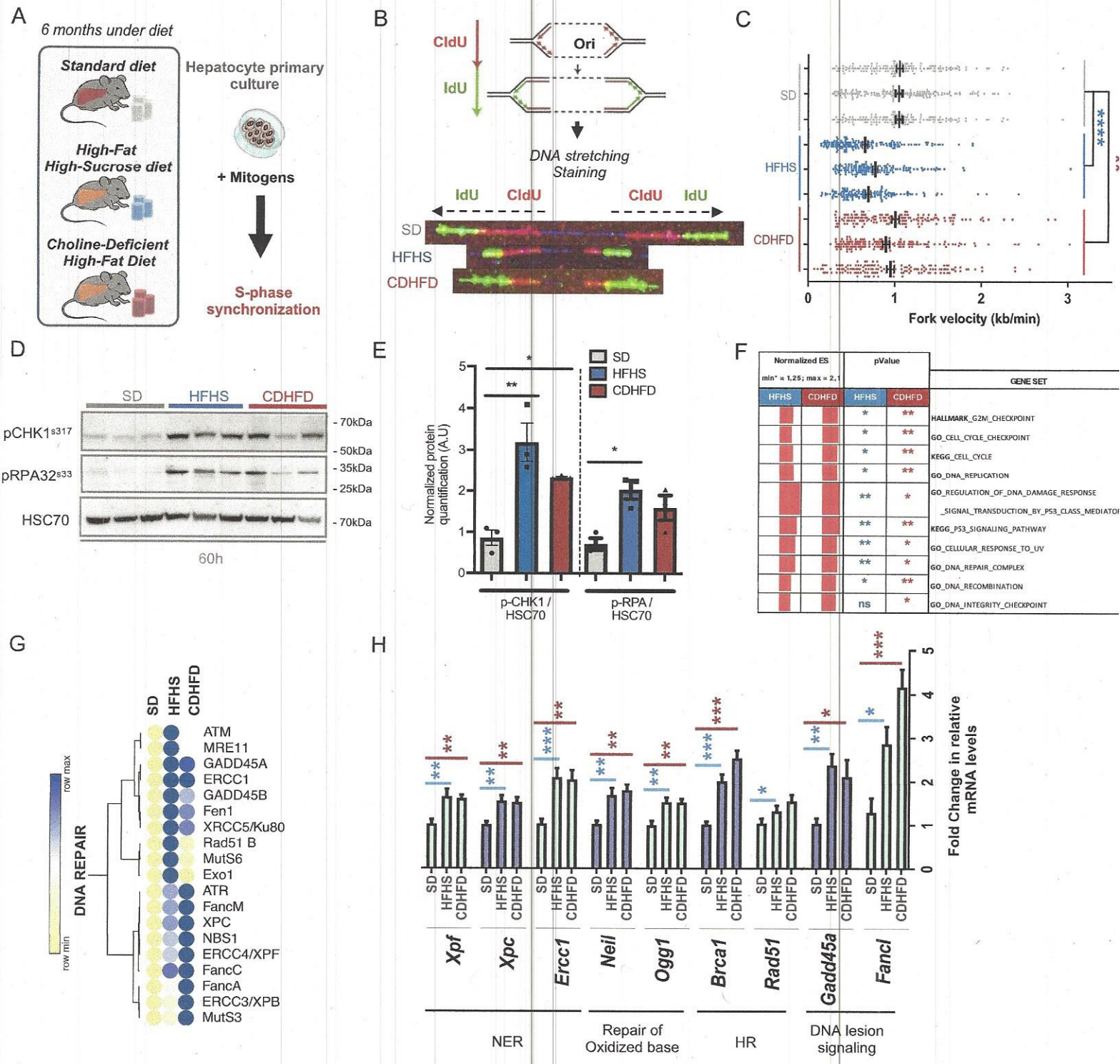
A
6 months under diet
Standard diet
High-Fat High-Sucrose diet
Choline-Deficient High-Fat Diet
Hepatocyte primary culture
+ Mitogens
S-phase synchronization
B
CldU
IdU
Ori
DNA stretching
Staining
IdU CldU
CldU IdU
SD
HFHS
CDHFD
C
SD
HFHS
CDHFD
****
0 1 2 3
Fork velocity (kb/min)
D
SD HFHS CDHFD
pCHK1s317
pRPA32s33
HSC70
- 70kDa
- 50kDa
- 35kDa
- 25kDa
- 70kDa
60h
E
SD
HFHS
CDHFD
Normalized protein quantification (A.U)
p-CHK1 / HSC70
p-RPA / HSC70
F
Normalized ES
min* = 1,25; max = 2,1
pValue
GENE SET
HFHS CDHFD HFHS CDHFD
HALLMARK_G2M_CHECKPOINT
GO_CELL_CYCLE_CHECKPOINT
KEGG_CELL_CYCLE
GO_DNA_REPLICATION
GO_REGULATION_OF_DNA_DAMAGE_RESPONSE
_SIGNAL_TRANSDUCTION_BY_P53_CLASS_MEDIATOR
KEGG_P53_SIGNALING_PATHWAY
GO_CELLULAR_RESPONSE_TO_UV
GO_DNA_REPAIR_COMPLEX
GO_DNA_RECOMBINATION
GO_DNA_INTEGRITY_CHECKPOINT
G
SD HFHS CDHFD
row max
row min
DNA REPAIR
ATM
MRE11
GADD45A
ERCC1
GADD45B
Fen1
XRCC5/Ku80
Rad51 B
MutS6
Exo1
ATR
FancM
XPC
NBS1
ERCC4/XPF
FancC
FancA
ERCC3/XPB
MutS3
H
Fold Change in relative mRNA levels
SD HFHS CDHFD
Xpf
Xpc
Ercc1
Neil
Ogg1
Brca1
Rad51
Gadd45a
Fancl
NER
Repair of Oxidized base
HR
DNA lesion signaling

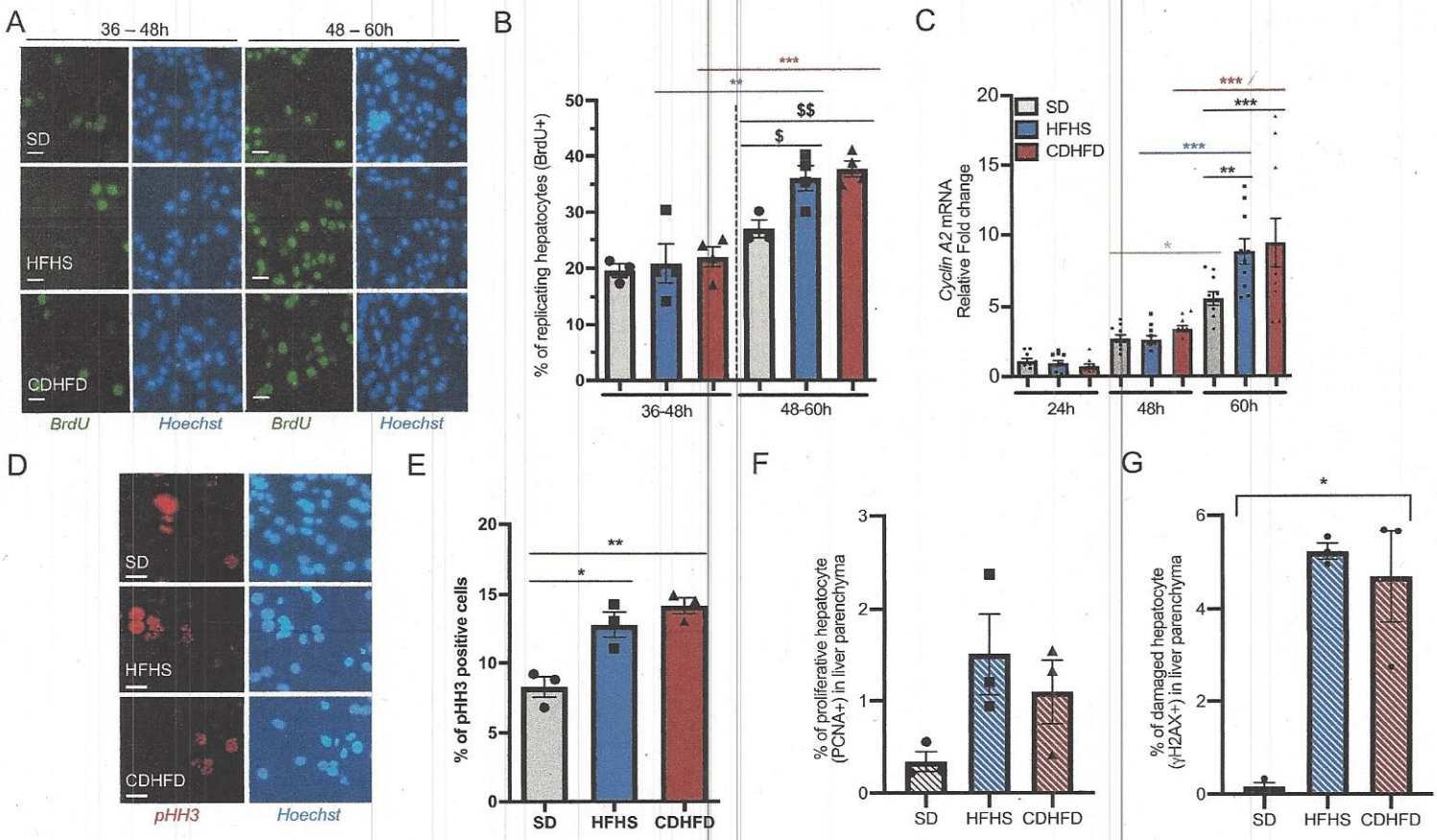
A
36 – 48h
48 – 60h
SD
HFHS
CDHFD
BrdU
Hoechst
BrdU
Hoechst
B
% of replicating hepatocytes (BrdU+)
36-48h
48-60h
C
SD
HFHS
CDHFD
Cyclin A2 mRNA
Relative Fold change
24h
48h
60h
D
SD
HFHS
CDHFD
pHH3
Hoechst
E
% of pHH3 positive cells
SD
HFHS
CDHFD
F
% of proliferative hepatocyte
(PCNA+) in liver parenchyma
SD
HFHS
CDHFD
G
% of damaged hepatocyte
(γH2AX+) in liver parenchyma
SD
HFHS
CDHFD

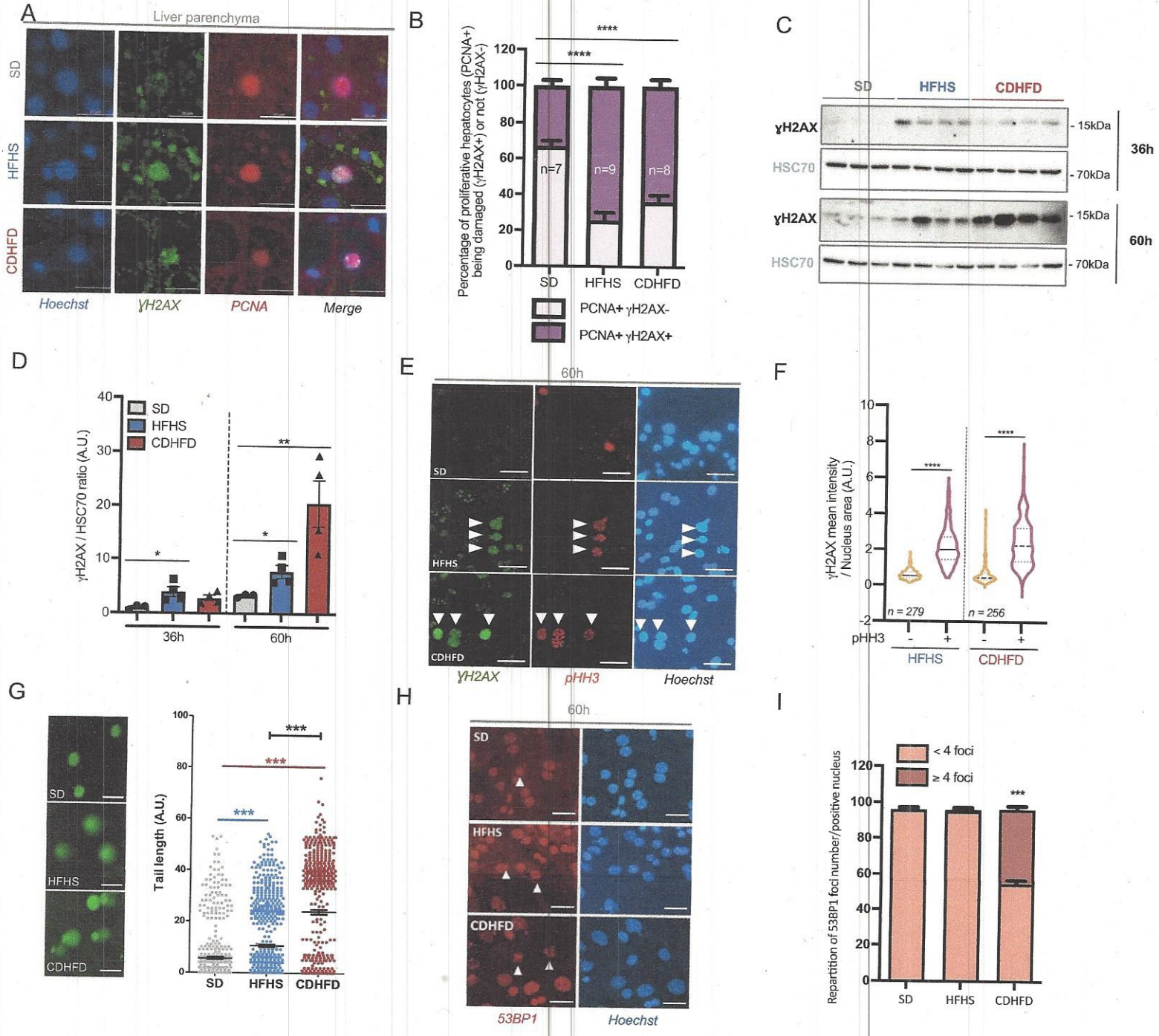
A
Liver parenchyma
SD
HFHS
CDHFD
Hoechst
γH2AX
PCNA
Merge
B
Percentage of proliferative hepatocytes (PCNA+) being damaged (γH2AX+) or not (γH2AX-)
****
****
n=7
n=9
n=8
SD
HFHS
CDHFD
PCNA+ γH2AX-
PCNA+ γH2AX+
C
SD
HFHS
CDHFD
γH2AX
HSC70
15kDa
70kDa
36h
60h
D
γH2AX / HSC70 ratio (A.U.)
SD
HFHS
CDHFD
36h
60h
E
60h
SD
HFHS
CDHFD
γH2AX
pHH3
Hoechst
F
γH2AX mean intensity / Nucleus area (A.U.)
n = 279
n = 256
pHH3
HFHS
CDHFD
G
SD
HFHS
CDHFD
Tail length (A.U.)
H
60h
SD
HFHS
CDHFD
53BP1
Hoechst
I
< 4 foci
≥ 4 foci
Repartition of 53BP1 foci number/positive nucleus
SD
HFHS
CDHFD

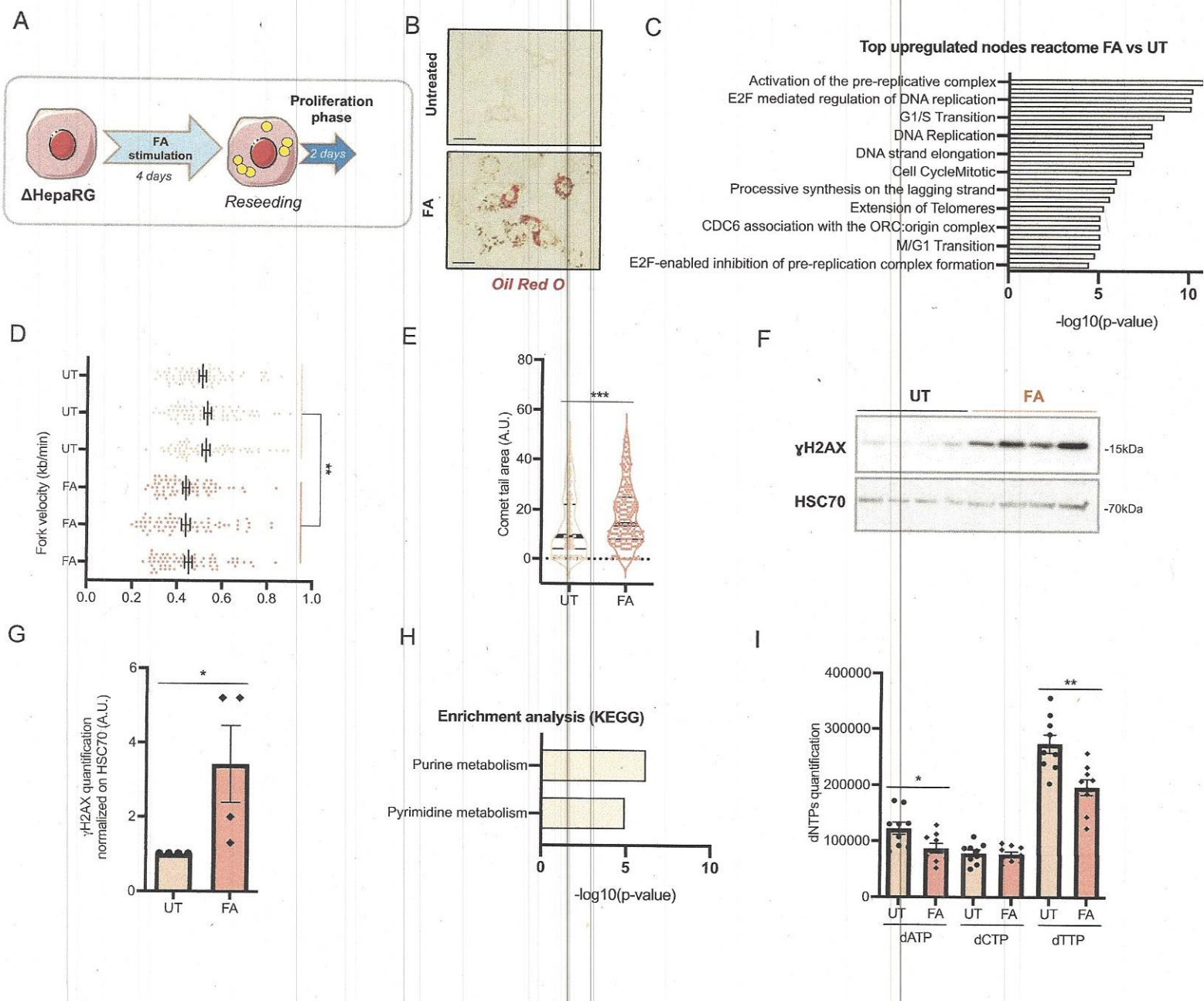
A
ΔHepaRG
FA stimulation
4 days
Reseeding
Proliferation phase
2 days
B
Untreated
FA
Oil Red O
C
Top upregulated nodes reactome FA vs UT
Activation of the pre-replicative complex
E2F mediated regulation of DNA replication
G1/S Transition
DNA Replication
DNA strand elongation
Cell CycleMitotic
Processive synthesis on the lagging strand
Extension of Telomeres
CDC6 association with the ORC:origin complex
M/G1 Transition
E2F-enabled inhibition of pre-replication complex formation
-log10(p-value)
D
Fork velocity (kb/min)
UT
FA
E
Comet tail area (A.U.)
***
F
UT
FA
γH2AX
HSC70
-15kDa
-70kDa
G
γH2AX quantification normalized on HSC70 (A.U.)
*
H
Enrichment analysis (KEGG)
Purine metabolism
Pyrimidine metabolism
-log10(p-value)
I
dNTPs quantification
dATP
dCTP
dTTP

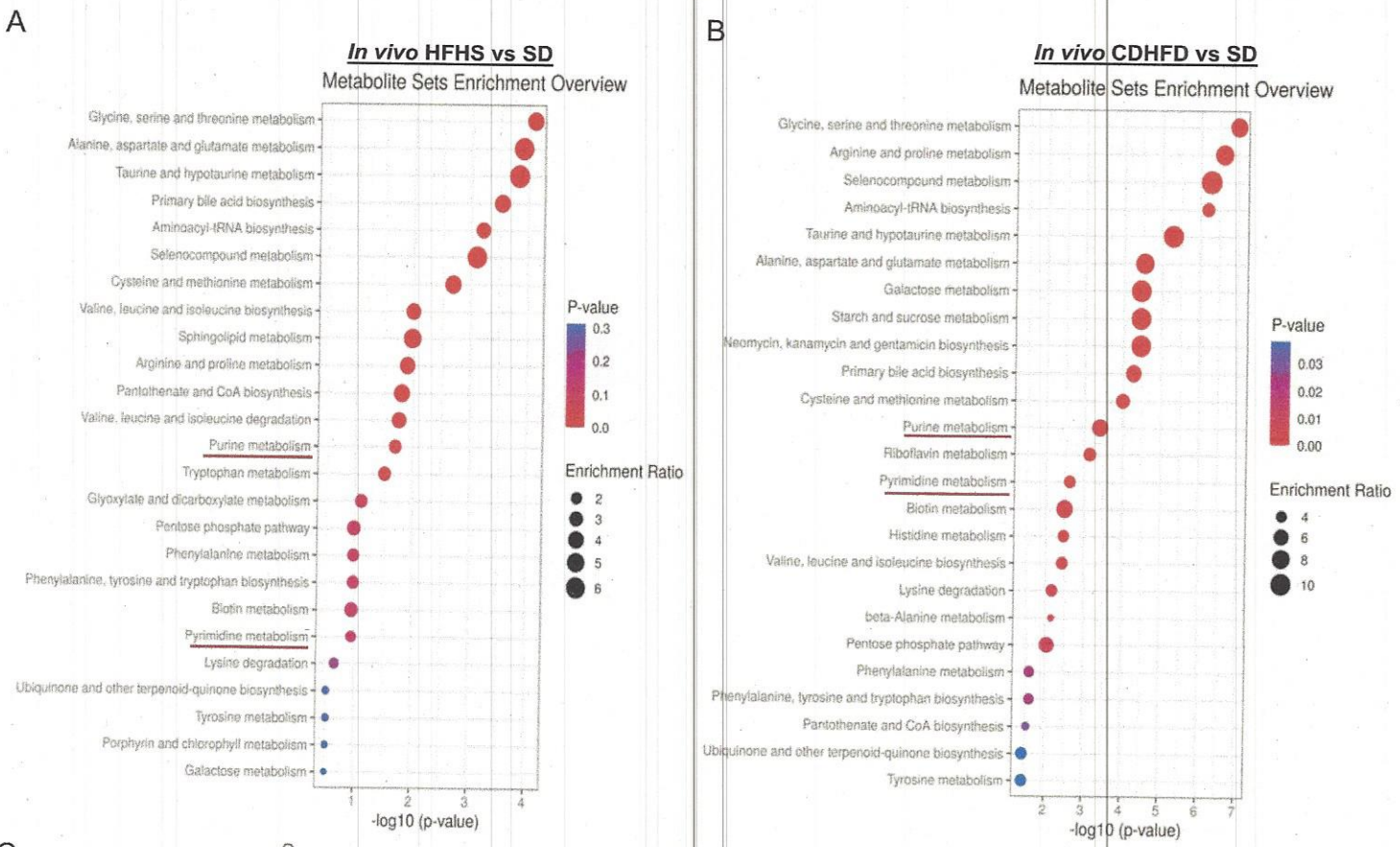
A
In vivo HFHS vs SD
Metabolite Sets Enrichment Overview
Glycine, serine and threonine metabolism
Alanine, aspartate and glutamate metabolism
Taurine and hypotaurine metabolism
Primary bile acid biosynthesis
Aminoacyl-tRNA biosynthesis
Selenocompound metabolism
Cysteine and methionine metabolism
Valine, leucine and isoleucine biosynthesis
Sphingolipid metabolism
Arginine and proline metabolism
Pantothenate and CoA biosynthesis
Valine, leucine and isoleucine degradation
Purine metabolism
Tryptophan metabolism
Glyoxylate and dicarboxylate metabolism
Pentose phosphate pathway
Phenylalanine metabolism
Phenylalanine, tyrosine and tryptophan biosynthesis
Biotin metabolism
Pyrimidine metabolism
Lysine degradation
Ubiquinone and other terpenoid-quinone biosynthesis
Tyrosine metabolism
Porphyrin and chlorophyll metabolism
Galactose metabolism
-log10 (p-value)
P-value
Enrichment Ratio
B
In vivo CDHFD vs SD
Metabolite Sets Enrichment Overview
Glycine, serine and threonine metabolism
Arginine and proline metabolism
Selenocompound metabolism
Aminoacyl-tRNA biosynthesis
Taurine and hypotaurine metabolism
Alanine, aspartate and glutamate metabolism
Galactose metabolism
Starch and sucrose metabolism
Neomycin, kanamycin and gentamicin biosynthesis
Primary bile acid biosynthesis
Cysteine and methionine metabolism
Purine metabolism
Riboflavin metabolism
Pyrimidine metabolism
Biotin metabolism
Histidine metabolism
Valine, leucine and isoleucine biosynthesis
Lysine degradation
beta-Alanine metabolism
Pentose phosphate pathway
Phenylalanine metabolism
Phenylalanine, tyrosine and tryptophan biosynthesis
Pantothenate and CoA biosynthesis
Ubiquinone and other terpenoid-quinone biosynthesis
Tyrosine metabolism
-log10 (p-value)
P-value
Enrichment Ratio

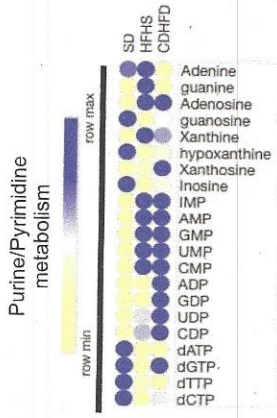
C
SD
HFHS
CDHFD
Purine/Pyrimidine metabolism
row max
row min
Adenine
guanine
Adenosine
guanosine
Xanthine
hypoxanthine
Xanthosine
Inosine
IMP
AMP
GMP
UMP
CMP
ADP
GDP
UDP
CDP
dATP
dGTP
dTTP
dCTP

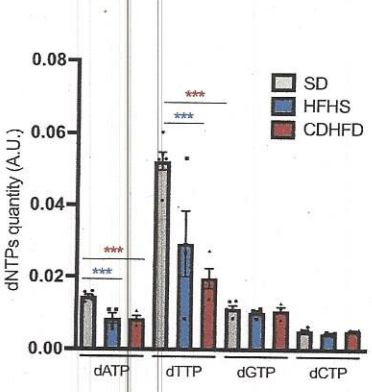
D
dNTPs quantity (A.U.)
SD
HFHS
CDHFD
dATP
dTTP
dGTP
dCTP

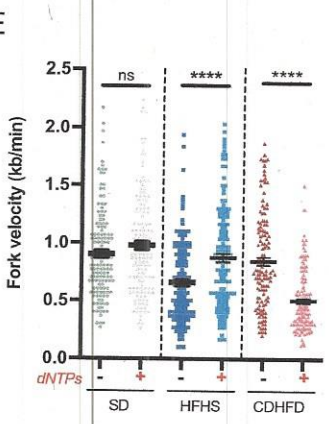
E
Fork velocity (kb/min)
ns
****
****
dNTPs
SD
HFHS
CDHFD

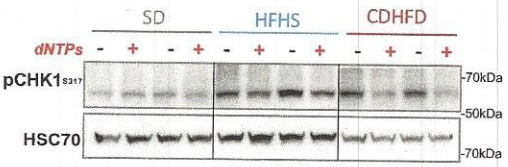
F
SD
HFHS
CDHFD
dNTPs
pCHK1 S317
HSC70
70kDa
50kDa
70kDa

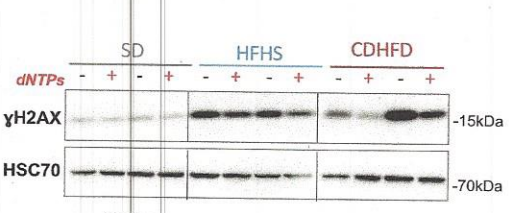
H
SD
HFHS
CDHFD
dNTPs
γH2AX
HSC70
15kDa
70kDa

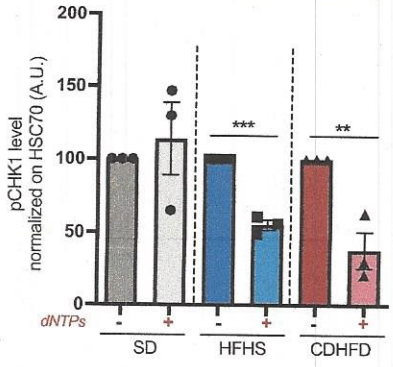
G
pCHK1 level normalized on HSC70 (A.U.)
dNTPs
SD
HFHS
CDHFD

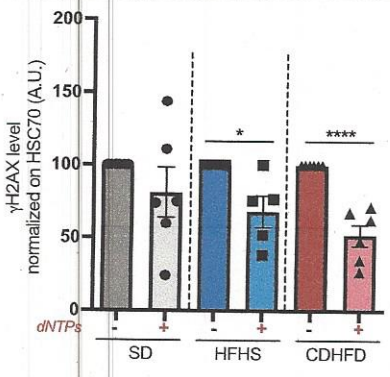
I
γH2AX level normalized on HSC70 (A.U.)
dNTPs
SD
HFHS
CDHFD

A

Normalized ES min* = -1,3 ; max = -1,8		pValue		GENE SET
HFHS	CDHFD	HFHS	CDHFD	
		**	*	GO_POSITIVE_REGULATION_OF_NUCLEOSIDE_METABOLIC_PROCESS
		*	*	GO_REGULATION_OF_NUCLEOSIDE_METABOLIC_PROCESS
		ns	**	GO_NUCLEOSIDE_MONOPHOSPHATE_METABOLIC_PROCESS
		*	*	GO_NUCLEOSIDE_BISPHOSPHATE_METABOLIC_PROCESS
		*	**	GO_NUCLEOSIDE_TRIPHOSPHATE_METABOLIC_PROCESS
		*	ns	GO_PURINE_RIBONUCLEOSIDE_BISPHOSPHATE_METABOLIC_PROCESS
		*	**	GO_PURINE_CONTAINING_COMPOUND_METABOLIC_PROCESS
		ns	**	GO_NUCLEOTIDE_PHOSPHORYLATION
		ns	*	GO_DEOXYRIBONUCLEOTIDE_METABOLIC_PROCESS

B

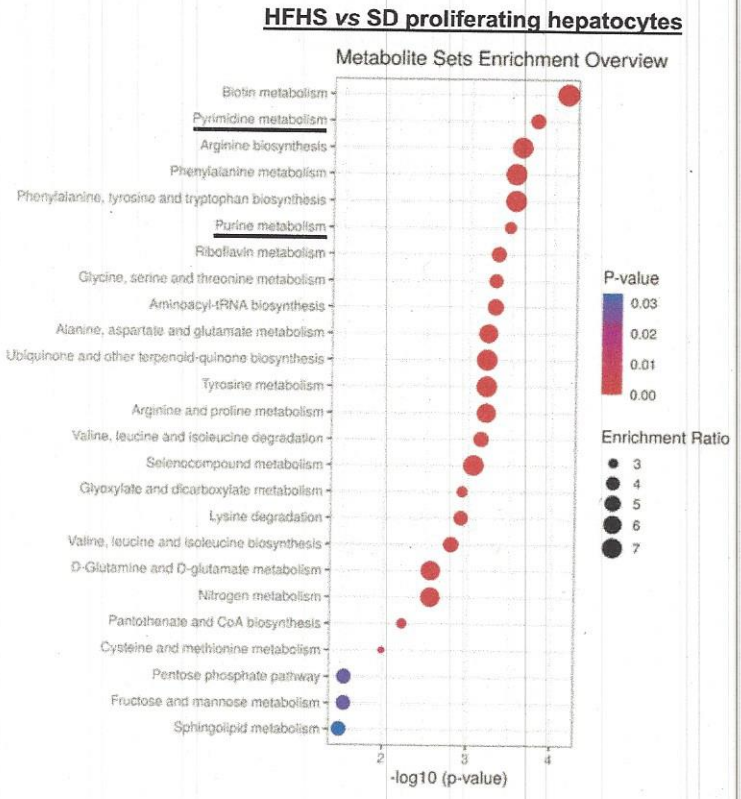

C

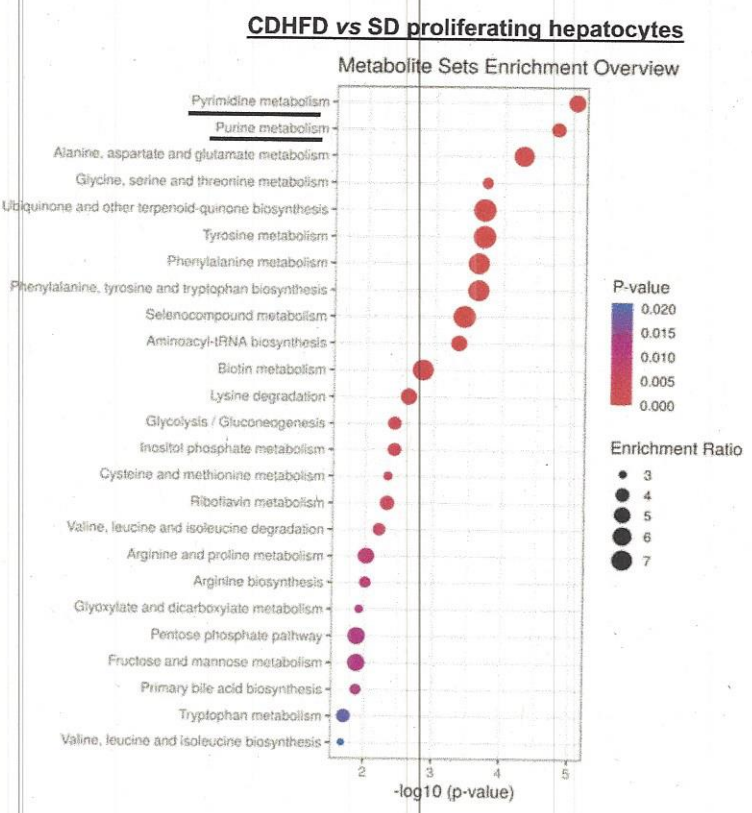

D

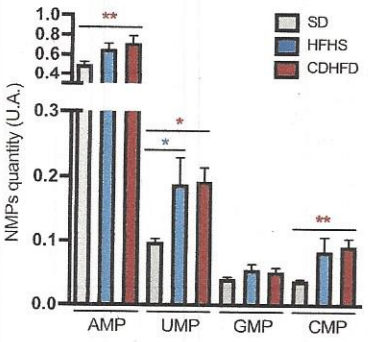

E

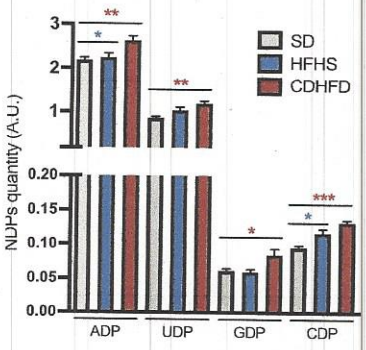

F

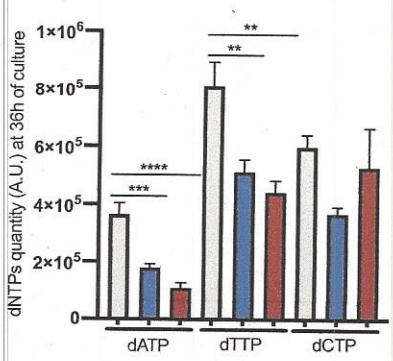

G

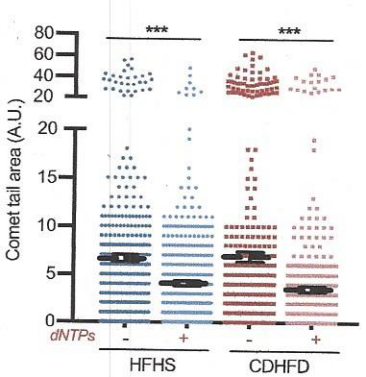

A

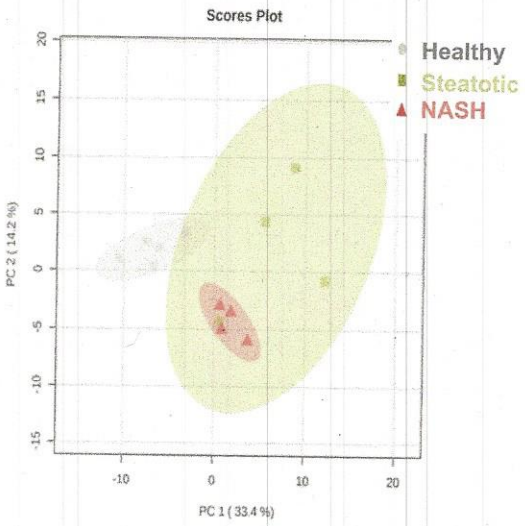
Scores Plot
Healthy
Steatotic
NASH
PC 2 (14.2 %)
PC 1 (33.4 %)

B

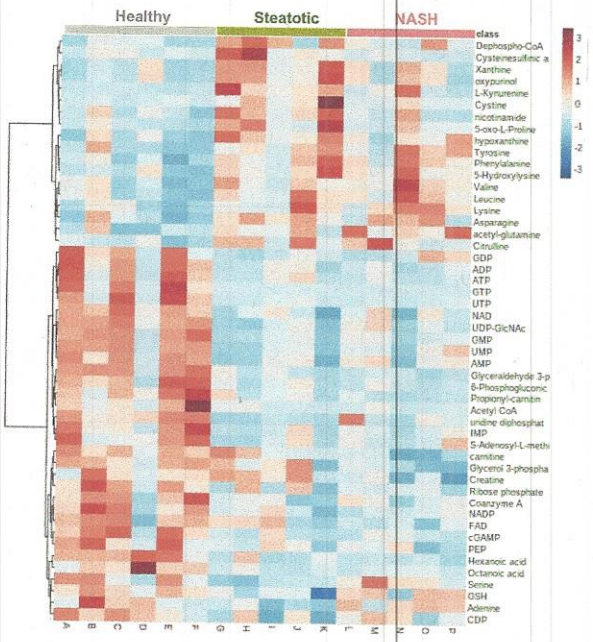
Healthy
Steatotic
NASH
class
Dephospho-CoA
Cysteinesulfinic a
Xanthine
oxypurinol
L-Kynurenine
Cystine
nicotinamide
5-oxo-L-Proline
hypoxanthine
Tyrosine
Phenylalanine
5-Hydroxylysine
Valine
Leucine
Lysine
Asparagine
acetyl-glutamine
Citrulline
GDP
ADP
ATP
GTP
UTP
NAD
UDP-GlcNAc
GMP
UMP
AMP
Glyceraldehyde 3-p
6-Phosphogluconic
Propionyl-carnitin
Acetyl CoA
uridine diphosphat
IMP
S-Adenosyl-L-meth
carnitine
Glycerol 3-phospha
Creatine
Ribose phosphate
Coenzyme A
NADP
FAD
cGAMP
PEP
Hexanoic acid
Octanoic acid
Serine
GSH
Adenine
CDP

C

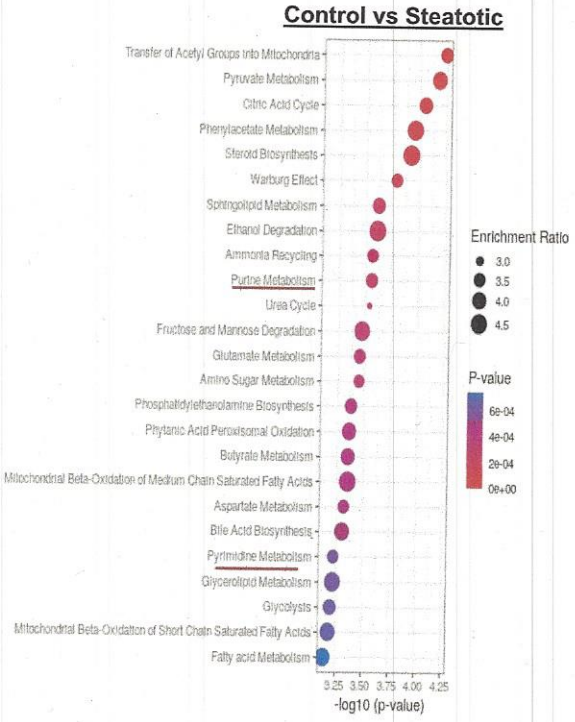
Control vs Steatotic
Transfer of Acetyl Groups into Mitochondria
Pyruvate Metabolism
Citric Acid Cycle
Phenylacetate Metabolism
Steroid Biosynthesis
Warburg Effect
Sphingolipid Metabolism
Ethanol Degradation
Ammonia Recycling
Purine Metabolism
Urea Cycle
Fructose and Mannose Degradation
Glutamate Metabolism
Amino Sugar Metabolism
Phosphatidylethanolamine Biosynthesis
Phytanic Acid Peroxisomal Oxidation
Butyrate Metabolism
Mitochondrial Beta-Oxidation of Medium Chain Saturated Fatty Acids
Aspartate Metabolism
Bile Acid Biosynthesis
Pyrimidine Metabolism
Glycerolipid Metabolism
Glycolysis
Mitochondrial Beta-Oxidation of Short Chain Saturated Fatty Acids
Fatty acid Metabolism
3.25 3.50 3.75 4.00 4.25
-log10 (p-value)
Enrichment Ratio
3.0
3.5
4.0
4.5
P-value
6e-04
4e-04
2e-04
0e+00

D

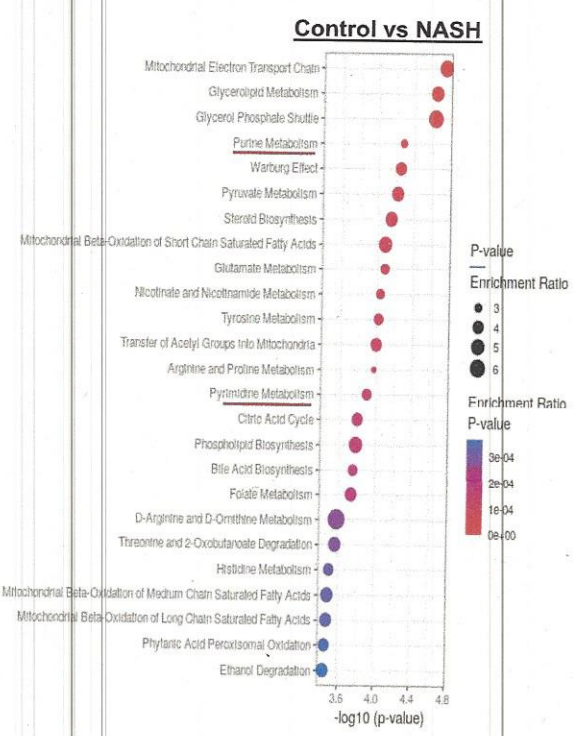
Control vs NASH
Mitochondrial Electron Transport Chain
Glycerolipid Metabolism
Glycerol Phosphate Shuttle
Purine Metabolism
Warburg Effect
Pyruvate Metabolism
Steroid Biosynthesis
Mitochondrial Beta-Oxidation of Short Chain Saturated Fatty Acids
Glutamate Metabolism
Nicotinate and Nicotinamide Metabolism
Tyrosine Metabolism
Transfer of Acetyl Groups into Mitochondria
Arginine and Proline Metabolism
Pyrimidine Metabolism
Citric Acid Cycle
Phospholipid Biosynthesis
Bile Acid Biosynthesis
Folate Metabolism
D-Arginine and D-Ornithine Metabolism
Threonine and 2-Oxobutanoate Degradation
Histidine Metabolism
Mitochondrial Beta-Oxidation of Medium Chain Saturated Fatty Acids
Mitochondrial Beta-Oxidation of Long Chain Saturated Fatty Acids
Phytanic Acid Peroxisomal Oxidation
Ethanol Degradation
3.6 4.0 4.4 4.8
-log10 (p-value)
P-value
Enrichment Ratio
3
4
5
6
Enrichment Ratio
P-value
3e-04
2e-04
1e-04
0e+00

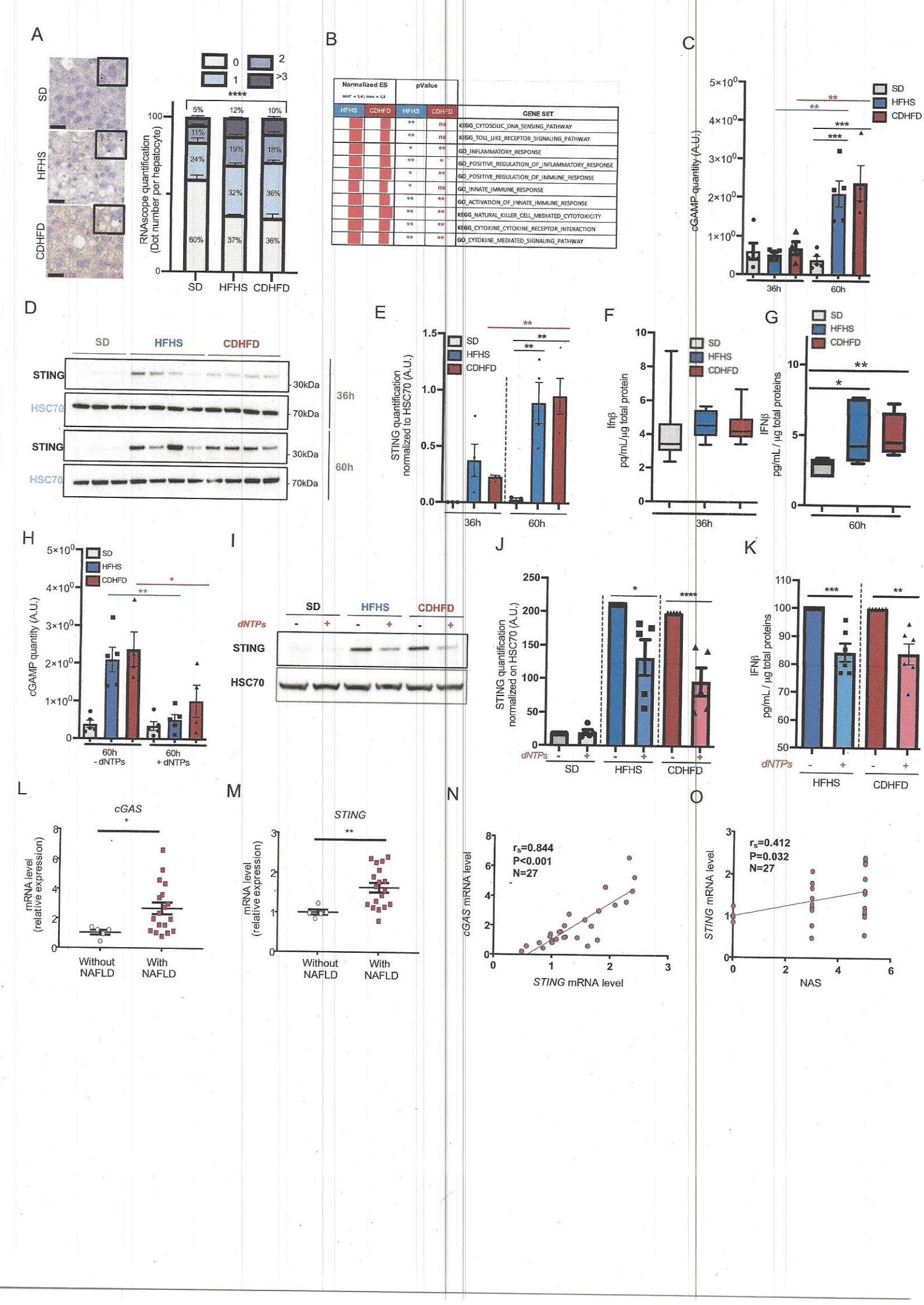
A
SD
HFHS
CDHFD
0
1
2
>3
****
RNAscope quantification (Dot number per hepatocyte)
5%
12%
10%
11%
24%
19%
32%
18%
36%
60%
37%
36%
SD
HFHS
CDHFD
B
Normalized ES
pValue
HFHS
CDHFD
GENE SET
KEGG_CYTOSOLIC_DNA_SENSING_PATHWAY
KEGG_TOLL_LIKE_RECEPTOR_SIGNALING_PATHWAY
GO_INFLAMMATORY_RESPONSE
GO_POSITIVE_REGULATION_OF_INFLAMMATORY_RESPONSE
GO_POSITIVE_REGULATION_OF_IMMUNE_RESPONSE
GO_INNATE_IMMUNE_RESPONSE
GO_ACTIVATION_OF_INNATE_IMMUNE_RESPONSE
KEGG_NATURAL_KILLER_CELL_MEDIATED_CYTOTOXICITY
KEGG_CYTOKINE_CYTOKINE_RECEPTOR_INTERACTION
GO_CYTOKINE_MEDIATED_SIGNALING_PATHWAY
C
cGAMP quantity (A.U.)
SD
HFHS
CDHFD
36h
60h
D
SD
HFHS
CDHFD
STING
HSC70
30kDa
70kDa
36h
60h
E
STING quantification normalized to HSC70 (A.U.)
F
Ifnβ pg/mL/µg total protein
G
IFNβ pg/mL / µg total proteins
H
cGAMP quantity (A.U.)
60h - dNTPs
60h + dNTPs
I
dNTPs
J
STING quantification normalized on HSC70 (A.U.)
K
IFNβ pg/mL / µg total proteins
L
cGAS
mRNA level (relative expression)
Without NAFLD
With NAFLD
M
STING
N
cGAS mRNA level
STING mRNA level
rs=0.844
P<0.001
N=27
O
STING mRNA level
NAS
rs=0.412
P=0.032
N=27

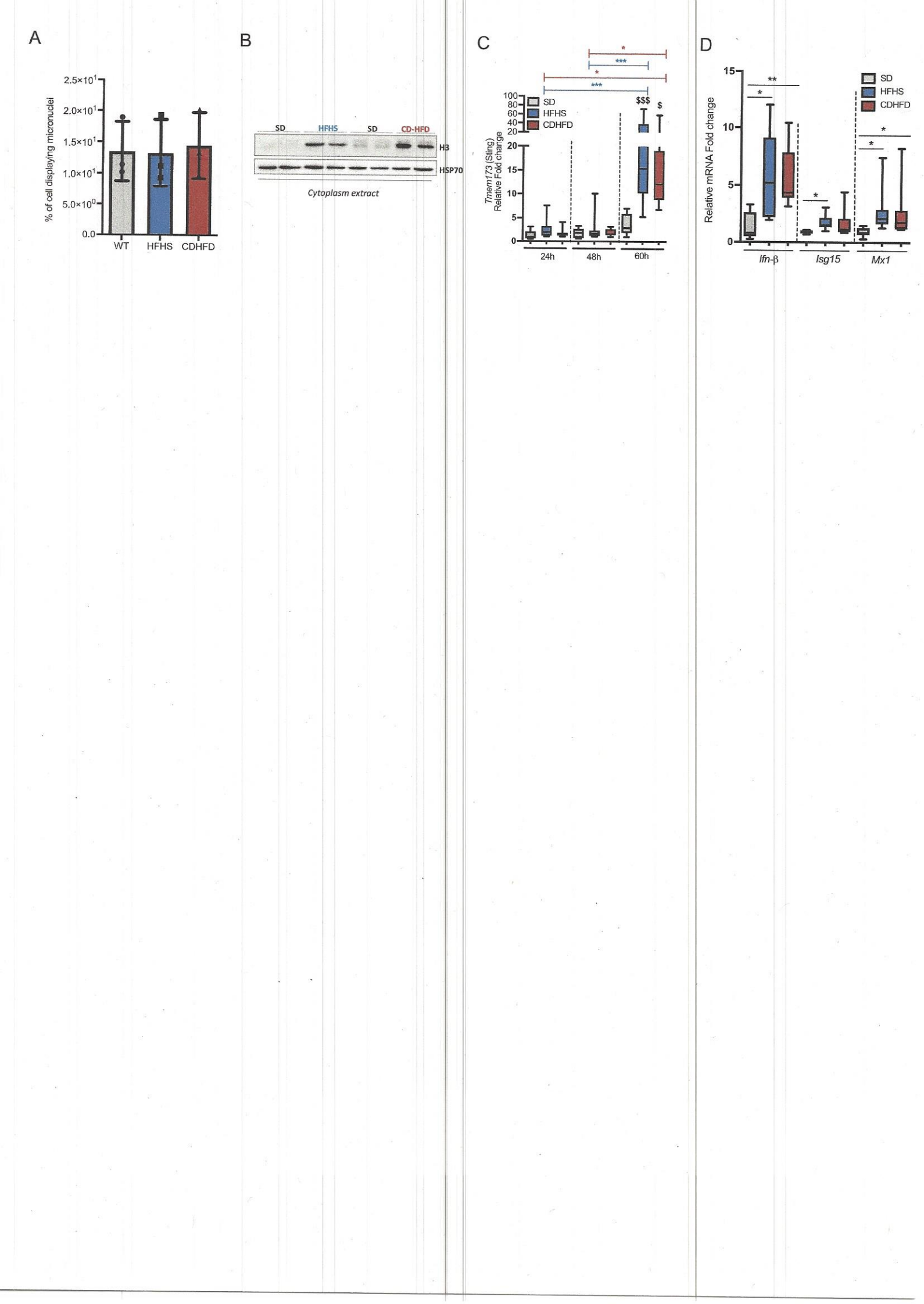
A
% of cell displaying micronuclei
2.5×10¹
2.0×10¹
1.5×10¹
1.0×10¹
5.0×10⁰
0.0
WT
HFHS
CDHFD
B
SD
HFHS
SD
CD-HFD
H3
HSP70
Cytoplasm extract
C
Tmem173 (Sting)
Relative Fold change
100
80
60
40
20
SD
HFHS
CDHFD
$$$
$
20
15
10
5
0
24h
48h
60h
D
Relative mRNA Fold change
15
10
5
0
SD
HFHS
CDHFD
Ifn-β
Isg15
Mx1